The MUSCLES Extension for Atmospheric Transmission Spectroscopy

Patrick R. Behr (ID)[1]

[1] *University of Colorado, Boulder, CO*

ABSTRACT

X-ray through infrared SEDs are essential for understanding a star's effect on exoplanet atmospheric composition and evolution. We present a catalog of panchromatic SEDs for 11 exoplanet hosting stars which have guaranteed *JWST* observation time as part of the ERS or GTO programs but have no previous UV characterization. The stars in this survey range from spectral type M6-F4 (0.14-1.57$M_\odot$) and ∼4-132 days in rotation period (∼0.5-11.4Gyr in age). The SEDs are composite spectra using data from the *Chandra X-ray Observatory* and *XMM-Newton*, the *Hubble Space Telescope*, BT-Settl stellar atmosphere models, and scaled spectra of proxy stars of similar spectral type and activity. From our observations, we have measured a set of UV and X-ray fluxes as indicators of stellar activity level. We compare the chromospheric and coronal activity indicators of our exoplanet-hosting stars to the broader population field stars and find that a majority of our targets have activity levels lower than the average population of cool stars in the solar neighborhood. This suggests that using SEDs of stars selected from exoplanet surveys to compute generic exoplanet atmosphere models may be underestimating the host star's UV flux by an order of magnitude or more and consequently that the observed population of exoplanetary atmospheres receive lower high-energy flux levels than the typical planet in the solar neighborhood.

Keywords: stars: chromospheres — planets: atmospheres — ultraviolet: stars

1. INTRODUCTION

The NASA exoplanet archive lists over 5000 confirmed exoplanets across nearly 4000 distinct systems as of August, 2022. Estimates from *Kepler* observations predict exoplanet occurance rates around F-, G-, and K-type stars of ∼ 10 − 60% (Kunimoto & Bryson 2020; Fressin et al. 2013; Traub 2012; Kopparapu 2013) and up to 80% or more for M dwarf stars (Bryson et al. 2020; Dressing & Charbonneau 2015). As the number of confirmed exoplanets increases, so too does the opportunity to characterize the composition and evolution of exoplanetary atmospheres. Atmospheric transmission spectroscopy with the *James Webb Space Telescope* (JWST) will provide the highest quality observations to date of exoplanetary atmospheres. These observations will allow characterization of atmospheric composition and modeling of aerosol and haze formation (Bean et al. 2018; Kawashima et al. 2019). The UV spectrum of a planet's host star drives photochemistry in exoplanetary atmospheres, which in turn controls the overall composition of the atmosphere (Miguel & Kaltenegger 2014; Miguel et al. 2015; Moses et al. 2011; Venot et al. 2013), the formation of photochemical hazes and aerosols (He et al. 2018; Kawashima & Ikoma 2018; Kawashima et al. 2019), and powers atmospheric escape in both gaseous and terrestrial planets (Johnstone et al. 2015; Vidal-Madjar et al. 2004; Murray-Clay et al. 2009). Thus, knowledge of the host star's UV spectrum is critical to the interpretation of current and future exoplanet atmosphere observations.

1.1. *Stellar UV effects on atmospheric chemistry of Neptune to Jupiter sized planets*

The atmospheres of extrasolar giant planets, like the gas giant planets of our own solar system, are primarily H_2 and He dominated. Oxygen, nitrogen, and carbon are typically contained in H_2O, N_2, and CO for hot planets with T$\gtrsim$ 700K (Burrows & Orton 2010; Madhusudhan et al. 2016; Fortney et al. 2021). These molecular reservoirs all have photodissociation cross sections in the UV, typically peaking at less than 1300Å (Loyd et al. 2016). Thus, in the upper atmosphere of these planets, photochemical effects from UV irradiation can dominate the atmospheric composition, destroying NH_3, N_2, CO, CH_4, and H_2O, and leading to buildups of H, HCN, C_2H_2, N, and C (Moses et al. 2011;

Line et al. 2010; Zahnle et al. 2009; Miguel & Kaltenegger 2014). There is also evidence that increased UV radiation plays a role in creating the observed temperature inversion in hot-Jupiter atmospheres, where temperature increases with altitude, forming a type of stratosphere (Fu et al. 2022; Lothringer & Barman 2019; Zahnle et al. 2009; Knutson et al. 2010).

The > 5000 confirmed exoplanets so far exhibit a wide range of masses, from sub-Earth to tens of Jupiter masses, as well as orbital periods ranging from hours to tens of years. However, there is a notable dearth of Neptune-mass planets ($0.03 \lesssim M/M_{jup} \lesssim 0.3$) with short orbital periods of $\lesssim 5d$, known as the "Neptune-desert" (Szabó & Kiss 2011; Mazeh et al. 2016). Owen & Lai (2018) propose that a combination of high-eccentricity migration and photoevaporation can explain the presence of this desert. In order to quantify photoevaporation processes, we must understand the UV irradiation experienced by the exoplanet. EUV radiation, elevated by the small semi-major axes of these planets, is capable of heating the atmosphere to temperatures up to $\sim 10^4$K, driving thermal mass loss via hydrodynamic escape (Yelle et al. 2008; Murray-Clay et al. 2009; Owen & Jackson 2012; Sanz-Forcada et al. 2011). On highly irradiated giant planets, the outflow may be sufficiently rapid that heavy elements are dragged along via collisions with hydrogen (Vidal-Madjar et al. 2004; Linsky et al. 2010; Ballester & Ben-Jaffel 2015; Koskinen et al. 2013). EUV driven hydrodynamic escape is particularly relevant for close-orbiting super-Earth to Neptune sized planets, potentially leading to complete evaporation of their gaseous envelopes on Gyr timescales, while Jupiter sized planets are more likely to retain their envelope over these timescales (Owen & Jackson 2012; Owen & Wu 2016; Fossati et al. 2017).

1.2. *Effect of UV irradiation on terrestrial planets and habitability*

UV radiation also directly affects the observable features of terrestrial exoplanetary atmospheres. For example, atmospheric transmission spectra of the super-Earth GJ 1214b with the *HST* Wide Field Camera 3 (WFC3) have revealed a "flat" transmission spectrum from $\sim 0.78 - 1.7\mu$m; that is, the spectrum is missing the strong absorption features due to H_2O and other molecules Bean et al. (2010); Berta et al. (2012). Kreidberg et al. (2014) concluded that the spectrum is inconsistent with a high molecular weight ($> 50\% \ H_2O$) atmosphere, arguing that the featureless spectrum must be a result of optically thick clouds or photochemical hazes, a direct result of UV irradiation. For sub- to super-Earth planets with tempertures $\lesssim 700$K, the dominant elemental reservoirs are H_2O, NH_3, and CH_4 (Burrows & Orton 2010; Madhusudhan et al. 2016; Fortney et al. 2021). UV radiation from a planet's host star penetrates the upper atmosphere, photodissociating CH_4, and initiates photochemical reactions leading to the formation of opaque organic molecules which can cause the observed flat transmission spectra (Linsky 2019; Arney et al. 2017; Miller-Ricci Kempton et al. 2012).

Remote sensing of exoplanet habitability relies heavily on the detection of gaseous biosignatures, particularly O_2, O_3, CO, and CH_4, but also including other hydrocarbons and N and S based gases (Segura et al. (2005); Des Marais et al. (2002); see section 4 of Schwieterman et al. (2018) for an extensive overview of gaseous biosignatures). However, as with the giant planets discussed above, the UV radiation input from the host star has a significant effect on the evolution of terrestrial planets' atmospheres. Molecular oxygen and ozone are readily detectable in the NUV, visible, and mid-IR and have the potential to be strong indicators of biologic activity. On Earth, O_3 is the direct result of photochemical processes splitting O_2 which is almost entirely sourced via oxygenic photosynthesis (Des Marais et al. 2002; Kiang et al. 2007). EUV and FUV radiation shortward of ~ 1800Å—especially in the Lyman-α emission line, which can comprise $\sim 37 - 75\%$ of the total FUV flux for M dwarfs (France et al. 2013)—photodissociates CO_2 and H_2O leading to escape of H and buildup of O and O_2 (Gao et al. 2015; Hu et al. 2012; Burkholder et al. 2015). Atmospheric oxygen chemistry can be described by the Chapman mechanism (Chapman 1930), where O_3 is produced by FUV photolysis of O_2:

$$O_2 + h\nu_{_{FUV}} \rightarrow O + O$$
$$O + O_2 + M \rightarrow O_3 + M$$
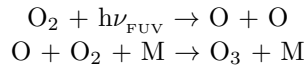
where M is a third body which can carry excess energy. NUV and blue-optical photolysis then causes the destruction of O_3 and buildup of O_2:

$$O_3 + h\nu_{_{NUV}} \rightarrow O_2 + O$$
$$O + O_3 \rightarrow O_2 + O_2$$
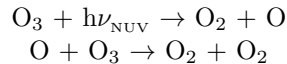
Thus, the ratio of FUV/NUV flux becomes critical for oxygen chemistry in the atmosphere; if a host star produces a large amount of FUV and relatively little NUV flux, a substantial O_3 atmosphere may arise entirely via photochemical

processes (Segura et al. 2010; Hu et al. 2012; Tian et al. 2014; Domagal-Goldman et al. 2014; Gao et al. 2015; Schwieterman et al. 2018). Additionally, the location of the habitable zone, the region around a star where liquid water is possible on the surface of a rocky planet, is dependent on atmospheric H escape, CO_2 and O_3 composition, and incident stellar flux—which are in turn related to the stellar luminosity and SED of the host star (Kasting et al. 1993; Kaltenegger 2017).

1.3. *UV time variability of cool stars*

Variability of UV radiation from a host star is critical to photochemistry and atmospheric stability of exoplanets. Solar EUV flux varies by factors up to ~ 100 on minute timescales during intense flares (Woods et al. 2012). In G-, K-, and M stars, quiescent FUV radiation is emission line dominated but continuum emission can become the dominant UV luminosity source during stellar flares (Kowalski et al. 2010; Loyd et al. 2018). M and K dwarfs in particular exhibit regular flare activity, even in old and inactive stars, and the energy released during these events may account for more FUV flux than the quiescent emission over stellar lifetimes (Loyd et al. 2018; France et al. 2020a). L 98-59, an M3 dwarf included in this survey, has received significant attention since the announcement of its 4 potentially terrestrial planets in 2019 (Pidhorodetska et al. 2021a; Kostov et al. 2019a; Barclay et al. 2021a). While L 98-59 is generally considered inactive (Astudillo-Defru et al. 2017; Cloutier et al. 2019), and therefore a good potential candidate for habitability studies, we observe two X-ray flares and one NUV flare separated by 24hrs (see Section 3.5). Flare frequency distributions of M dwarfs from Loyd et al. (2018) predict that flares of the size we observed on L 98-59 may happen up to tens of times per day. Such frequent high-energy flaring events could have dire consequences for planetary atmospheres. On the Sun, nearly all solar flares above a certain energy level are accompanied by a coronal mass ejection (CME) (Aarnio et al. 2011). These CMEs result in highly energic accelerated particles which impact planetary atmospheres, significantly enhancing pickup ions and leading to dramatic increases in atmospheric escape rate (Jakosky et al. 2015; Lammer et al. 2007; Airapetian et al. 2017). Furthermore, it has been shown that energetic particle deposition into the atmospheres of terrestrial planets can lead to significant changes in observable atmospheric oxygen abundances (Segura et al. 2010; Tilley et al. 2019). Thus, a combined knowledge of stellar flare rate and energy is necessary to allow estimates of lifetime-integrated UV flux experienced by exoplanets, especially those being assessed for their potential habitability.

1.4. *The MUSCLES and Mega-MUSCLES Treasury Surveys*

With the growth of exoplanetary science and the associated awareness of the importance of the host star's UV radiation field on the evolution of exoplanetary atmospheres, the community resources devoted to UV characterization of cool stars has increased (see, e.g., France et al. (2018)). This is particularly important since it has been shown that relying on empirical scaling is not sufficient to model the evolution of planetary atmospheres, and the extended UV continuum and UV emission lines are necessary to generate accurate models (Teal et al. 2022; Peacock et al. 2022). The MUSCLES Treasury Survey (*HST* Cycle 22; PI—France) began to address this dearth of observations by creating panchromatic 5Å-5.5μm SEDs of M and K dwarfs which have since been used extensively to study the importance of the UV radiation environment on exoplanets (for example,(Kawashima & Ikoma 2018; Lora et al. 2018; Chen et al. 2021)). The MUSCLES SEDs consist of observational spectra in the X-ray (5-50Å: *XMM-Newton* and *Chandra X-ray Observatory*) and UV (1170-5700Å: *HST*), high-quality empirical estimates of the EUV (50-1170Å) which cannot be presently observed owing to lack of an operating EUV observational facility (France et al. 2022), and stellar atmospheric models of the IR (5700Å-5.5μm) (Loyd et al. 2016). Stars in the MUSCLES survey covered a range of spectral types from K1V - M5V and all but one were considered "optically inactive" due to having Hα in absorption. Despite this classification, all showed chromospheric and coronal activity, showing that direct observations of host stars remains the gold standard for understanding effects of stellar irradiance on specific exoplanets (France et al. 2016).

The MUSCLES survey was subsequently expanded to include an additional 13 M dwarfs in the Mega-MUSCLES survey (*HST* Cycle 25; PI—Froning). Mega-MUSCLES has a particular focus on small ($M < 0.3 M_\odot$) stars with a range of spectral types from M8-M0, including Barnard's star and TRAPPIST-1 (Froning et al. 2019; Wilson et al. 2021; France et al. 2020b). Together, the MUSCLES and Mega-MUSCLES surveys provide an archive of SEDs which can be used as proxies for M and K dwarf planet hosts after *HST*'s lifetime and provide support for *JWST* observations of terrestrial planets around cool stars.

1.5. *The MUSCLES Extension for Atmospheric Spectroscopy*

The recent launch of *JWST* has begun an unprecedented era in exoplanet atmospheric characterization. Atmospheric spectroscopy of exoplanets ranging from Earth-sized terrestrial planets through giant hot-Jupiters will be obtained through a series of guaranteed transiting planet observations via the *JWST* Early Release Science (ERS) and Guaranteed Time Observations (GTO) programs. As described above, the high-energy SED of the host stars will be crucial to accurately interpret the results of these spectroscopic observations. We have identified 12 *JWST* guaranteed time targets which have no previous UV observations in the *HST* archive. The MUSCLES Extension for Atmospheric Spectroscopy extends the original MUSCLES survey over a larger range in stellar mass to include these 12 previously uncharacterized stars. Of the stars included in this survey we provide 11 panchromatic SEDs and an X-ray analysis of all 12. The stars in this work range from M6-F4 and host planets ranging from super-Earths to hot-Jupiters. We expand on the methods of the MUSCLES survey and create panchromatic SEDs of these stars, characterize them in relation to other known planet and non-planet hosting stars, and address selective bias towards observing low activity stars which may impact our interpretations of observed exoplanet atmospheres.

We structure the paper as follows: Section 2 describes the observational campaign, including *HST*, *Chandra*, and *XMM-Newton* observations, and the methods used to reconstruct the currently unobservable regions in the EUV. In section 3 we show the results of our observations and put them in context relative to the broader population of stellar surveys. We also discuss the importance of studying the time variability of host stars, spurred on by the detection of two X-ray flares in the star L 98-59. Finally, we summarize the main results of this work in section 4. A list of observed targets including particular observation details, SED construction, and descriptions of planetary systems can be found in Appendix A. Lists of X-ray and UV emission line fluxes can be found in Appendix B.

2. OBSERVATIONS

Observational data were obtained from *HST*, *Chandra*, and *XMM-Newton*. All *HST* observations were obtained through a dedicated observing program for this survey (*HST* Cycle 28, program ID 16166; PI—France), while *Chandra* and *XMM-Newton* were a combination of new and archived observations. In Table 1 we present a brief overview of each target in the MUSCLES Extension in order of descending effective temperature. For a detailed description of the planetary systems and their relation to the *JWST* ERS and GTO programs, as well as X-ray and UV data quality, major emission characteristics, and details of EUV proxy stars (see Section 2.5), we refer the reader to Appendix A.

Table 1: List of Targets

Star	Sp.Type	T_{eff} [K]	Distance [pc]	Mass [$M_\odot$]	Radius [$R_\odot$]	# of planets[a]
WASP-17	F4	6548	$405^{+8.779}_{-8.421}$	1.573 ± 0.092	1.306 ± 0.026	1
HD 149026	G0	6084	$75^{+0.174}_{-0.173}$	1.46 ± 0.08	1.34 ± 0.02	1
HAT-P-1	G0	6051	$158.979^{+0.977}_{-0.965}$	1.16 ± 0.11	$1.23^{+0.14}_{-0.10}$	1
WASP-127	G5	5828	$159^{+1.210}_{-1.191}$	1.31 ± 0.05	1.33 ± 0.03	1
WASP-77A	G8	5605	$105.166^{+1.209}_{-1.182}$	1.002 ± 0.045	0.955 ± 0.015	1
TOI-193	G7	5443	$80.4374^{+0.3174}_{-0.3150}$	$1.02^{+0.02}_{-0.03}$	0.949 ± 0.006	1
HAT-P-26	K1	5062	$141.837^{+1.152}_{-1.133}$	0.82 ± 0.03	$0.79^{+0.10}_{-0.04}$	1
HAT-P-12	K5	4653	$142.751^{+0.453}_{-0.450}$	0.730 ± 0.018	$0.701^{+0.017}_{-0.012}$	1
WASP-43	K7	4124	$86.7467^{+0.3281}_{-0.3257}$	0.717 ± 0.025	$0.667^{+0.010}_{0.011}$	1
L 678-39	M2.5	3490	9.442 ± 0.005	0.342 ± 0.011	0.337 ± 0.015	3
L 98-59	M3	3429	10.6194 ± 0.0032	0.313 ± 0.014	0.312 ± 0.014	4
LP 791-18	M6	2949	$26.4927^{+0.0640}_{-0.0638}$	0.139 ± 0.005	0.171 ± 0.018	2

[a]We report only the number of confirmed exoplanets

2.1. *FUV and NUV*

Unless otherwise stated, we refer to FUV as 912Å $< \lambda <$ 1700Å and NUV as 1700Å $< \lambda <$ 3200Å. We employed the STIS G140L and G230L gratings for the FUV & NUV continuum and emission lines, repsectively, and the G140M grating for higher resolution spectra in the Lyman-α emission region. Finally, in order to calibrate the UV data to visible/IR photospheric models and ground-based spectra, we obtained optical observations using the STIS G430L grating. The exposure times were estimated based on the minimum amount of time required to achieve S/N $\simeq$ 10 per resolution element in the characteristic line and continuum regions, and we expected S/N $>$ 20 in the optical spectra. As we shall discuss in Section 3, the MUSCLES Extension targets were lower activity than expected and the S/N in the FUV was lower than those calculated in the observation proposal. In the NUV/optical, the S/N calculations were accurate and we did achieve $S/N > 20$ per resolution element. In total, our *HST* spectra typically span $\sim 1150 - 5500$Å.

There are some notable exceptions to the general observing strategy outlined above: first, for cool stars of spectral type K5 and lower, the required exposure time to obtain an adequate S/N was too long and we opted to exclude G140L and G140M observations. We were thus unable to acquire direct emission line measurements for these targets. Exceptions to this are the M dwarfs L 98-59, for which we obtained both G140L and G140M, and L 678-39, for which we obtained G140M. L 678-39 exceeded the bright object protection limits, and we thus utilized the COS G130M and G160M gratings rather than the STIS gratings. Similarly, HD 149026 was observed with STIS E230M rather than STIS G230L. WASP-52 suffered from a guide star acquisition failure and all *HST* data were rendered unusable.

We reduced the *HST* data as follows:

First, we examined all observations for pointing or data quality errors. Several observations (G140M: HD 149026, L 98-59, TOI-193; G140L: WASP-17; G230L: LP 791-18) had incorrect extraction regions during the X1DCORR routine, presumably due to low signal. We examined the flat fielded images to determine proper extraction regions and re-extracted them manually. We also found poor data quality flags on the blue end of the G430L CCD for all observations, typically spanning $\sim$ 100 pixels; these were mostly pixels that were flagged for having zero flux (ie: flag 16384 in the data quality array; see section 2.5 of Sohn et al. 2019). The FUV MAMA detectors did not show any serious data quality issues.

After screening the observations and removing portions with poor data quality, we proceeded to coadd the spectra for any target that had multiple observations with the same grating by using an average weighted by the total exposure time. During the coaddition process, we found that some observations with the same grating had slightly different wavelength bins. Rather than try to correct for these discrepancies, we interpolated each spectrum onto a common wavelength grid with $\Delta\lambda = 0.5$Å, oversampling the native resolution of the gratings. This process conserves the total observed flux while allowing us to perform a simple coaddition.

After performing the coaddition for each grating observation, we examined the final S/N of each and culled data that we considered to be of poor quality; we chose a S/N$>$ 3 per pixel to be the threshold for data to be usable in the final spectrum. This resulted in all of the continua of all G140L observations being too low S/N to include in the final spectra, although we do find emission lines above the S/N threshold for most targets. For targets with emission lines below the threshold, we report the RMS value of the background over the line region as an upper limit on the emission line flux. G230L spectra were typically low S/N on the blue end until $\sim 2000 - 2300$Å, depending on effective temperature, at which point the photospheric emission begins to pick up. G430L spectra were all above the S/N threshold after culling the poor data quality pixels on the blue end of the detector.

After cleaning and coadding the spectra, we measured the emission line fluxes of the seven lines listed in Table 4. For emission lines with S/N $>$ 3 per pixel, the reported flux is the integrated flux over the background-subtracted line region:

$$F_{ion} = \sum_{\lambda_0 - \delta\lambda}^{\lambda_0 + \delta\lambda} \Delta\lambda F_\lambda - \sum_{\lambda_0 - \delta\lambda}^{\lambda_0 + \delta\lambda} \Delta\lambda F_{cont} \tag{1}$$

where $\Delta\lambda$ is the spacing between adjacent data points, and F_{cont} is the continuum flux, estimated from a polynomial fit to the continuum on either side of the emission line. The integration width, $\delta\lambda$, was selected by hand for each line to accommodate varying line widths and was typically ~ 5Åfor the low resolution G140L grating.

For the Mg II doublet, which typically had much higher S/N than the FUV lines, we performed a Monte-Carlo integration of the background subtracted flux, integrating over both lines and assuming for each pixel a normally distributed flux centered at the observed STIS flux value with a standard deviation of the 1σ error from the observed STIS data. For stars with large photospheric absorption, the background was fit with a 2 degree polynomial, while

the background for cooler stars with no visible absorption were fit with a 1 degree polynomial. We report the Mg II flux and 1σ error as the mean and standard deviation of the integrated flux after 10,000 trial integrations.

2.2. X-ray data

The MUSCLES Extension included X-ray observations of 5 stars via *Chandra* observations and 8 via *XMM-Newton* observations. The observations were a combination of new observations obtained for this program as well as archival observations. Source X-ray spectra were extracted from a circular region encompassing 5 pixels around the proper motion corrected source location and an annular background region centered on the target location encompassing as much area as possible without including other sources. Some targets were close to the edge of the detector chip and a background region centered on the target would extend beyond the edges of the chip. In these cases, we used a circular background region from a nearby representative area. For *Chandra* data we use the dmlist routine to obtain background subtracted count rates. For *XMM-Newton* observations, we use the Scientific Analysis System (SAS 20.0.0; Gabriel et al. (2004)) with the standard procedure and filters. Photon events were limited to those with an energy range of 0.3-10keV to remove spurious high-energy particle events. Three of five observations with the *Chandra* ACIS-S detector were found to be non-detections. *XMM-Newton* observations using the EPIC pn detector had four of eight non-detections. The observation of L 98-59 was found to have a large X-ray flare which began early in the observation and continued throughout the entire duration. This X-ray flare is discussed in further detail in section 3.5. We obtained X-ray fluxes over the 0.3-10keV energy range by using the observed count rate for detections in the PIMMS software assuming an APEC plasma model with logT of 6.55 (0.3058keV) and a fixed solar abundance. For non-detected sources, we use the total exposure time to calculate the theoretical count rate which would produce a $3-\sigma$ detection and use that count rate in PIMMS to generate an upper limit flux. At the energies observed, we found the H I column density to be negligible in computing the final flux.

2.3. Lyman-α

The Lyman-α emission line is heavily attenuated by the ISM, with the entire core of the line being unobservable for even the nearest stars, leaving only the wings of the line observed. Lyman-α flux plays an important role in the photochemistry of exoplanet atmospheres and therefore it is crucial to properly reconstruct the intrinsic line profile in order to accurately model atmospheric chemistry and constrain the potential for abiotic biosignatures (Miguel et al. 2015; Arney et al. 2017). Youngblood et al. (2022) have developed a method of reconstructing the intrinsic Lyman-α flux using MCMC methods to simultaneously fit the wings of the Lyman-α emission which remain after geocoronal subtraction as well as the ISM absorption. The functional form of the intrinsic line profile is a Voigt emission profile with a self-reversal that follows the shape of the emission:

$$F_{emission}^{\lambda} = \mathcal{V}^{\lambda} \cdot \exp\left(-p\mathcal{V}_{norm}^{\lambda}\right) \tag{2}$$

where $\mathcal{V}^{\lambda}$ is the Voigt emission profile, p the self-reversal parameter, and $\mathcal{V}_{norm}^{\lambda}$ the peak-normalized Voigt profile.

For MUSCLES Extension targets which had G140M observations with good S/N, we used the methods of Youngblood et al. (2022) to reconstruct the intrinsic Lyman-α emission line and use the reconstructed line for the region of $\sim 1212 - 1220$Å in the final SEDs. For targets where G140M observations were not feasible or the S/N was not sufficient to fit with the MCMC method, we estimated the total Lyman-α flux by using a power-law relation to the total Mg II $\lambda2800$ surface flux (Wood et al. 2005; Youngblood et al. 2016). After estimating the Lyman-α flux based on the Mg II relation, we create an intrinsic line profile of the form given by equation (2) by selecting a fixed self-reversal parameter and iterating through a range of amplitudes until the integrated flux of the self-reversed Voigt profile matches the flux estimated by the Mg II relation. The self-reversal parameter was chosen to be 1.5 for M type stars, 2.0 for K, and 2.4 for G and F types based on the results from (Youngblood et al. 2022). The reconstructed profiles match the estimated flux to within 0.05%.

Figure 1 shows a reconstructed profile for two stars; HD 149026, for which the G140M observation was sufficient to fit with the MCMC method, and WASP-77A, for which we used the Mg II flux estimation. The WASP-77A spectrum exhibits both large negative fluxes and spurious peak towards the line center; this is a result of poor background subtraction of geocoronal Lyman-α due to low S/N.

2.4. Visible through IR
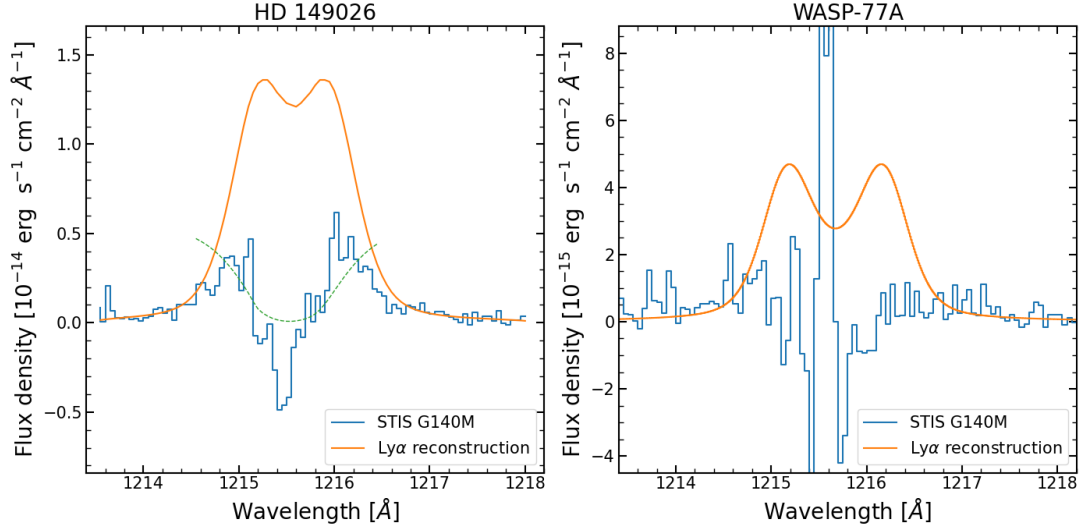
Figure 1: Left: Lyman α reconstruction for HD 149026 using the Youngblood et al. (2022) MCMC method. The green dashed line represents the transmission factor due to ISM absorption; the smaller values towards the line core are more heavily attenuated than the wings. Right: Lyman α reconstruction for WASP-77A using the Mg II flux estimation method.

The G430L spectra extend into visible wavelengths up to 5700Å. After this point, we have used the BT-Settl stellar atmosphere models (Allard et al. 2011) to extend the SEDs into the IR up to 5.5μm. The BT-Settl models cover a grid of effective temperatures (T$_{\text{eff}}$) and surface gravity (log g) and provide a flux observed at Earth based on stellar radius and distance. We scale the BT-Settl model to the NUV spectra from G430L as follows:

First, we convolve the high resolution BT-Settl model to match the resolution of the G430L data. We then take region > 5000Å where the BT-Settl model overlaps with the G430L spectrum and scale the model using a least-squares method. During the least-squares scaling procedure, we minimize the quantity $((F_{ref} - \alpha \times F_{proxy})/\sigma_{ref})^2$ where F_{ref} represents the G430L flux of the MUSCLES Extension target, F_{ref} the flux of the convolved BT-Settl model, α the scaling factor applied to the BT-Settl spectrum, and σ_{ref} the 1σ error of the observed G430L spectrum. The fits were examined by eye and found to be well representative of the shape of the observed spectra. Figure 2 shows the BT-Settl atmospheric model for 4100K < T$_{eff}$ < 4200K and 4.0 < log g < 4.5 scaled to the G430L spectrum of the K7 star WASP-43 using this method.

2.5. *EUV proxy stars*

The extreme ultraviolet (EUV) is heavily attenuated by the interstellar medium, particularly in the Lyman continuum region from the photoionization point of H at 912Å down to $\sim$ 200Å. Interstellar extinction, combined with the lack of an operating EUV observatory, means we currently do not have the ability to observe the EUV spectra of stars other than the Sun. We have therefore opted to use proxy stars of a similar spectral type and age as a substitute for the EUV spectra. Proxy star spectra were obtained from the publicly available MUSCLES (France et al. 2016) archives. The MUSCLES spectra used the *HST* COS to obtain UV measurements down to $\sim$ 1200Å, which yield higher S/N than our STIS observations, and EUV estimates based on their intrinsic Lyman-α fluxes (see Loyd et al. (2016); Youngblood et al. (2016)). After selecting a suitable proxy star, the proxy spectrum was scaled to the blue end of the NUV spectrum (G230L) via the same least-squares fitting method described in Section 2.4. We applied this routine to a region approximately 100Å wide where the proxy spectrum overlaps with the blue end of the observed G230L spectrum. The continua of the scaled proxy spectra match the continua of the observed STIS spectra within a 1σ error. Considering the importance of UV emission lines in atmospheric modeling, we replace the emission lines of the proxy spectra with the measured emission lines from our MUSCLES Extension observations; this provides the best balance between a representative continuum and ground-truth emission fluxes.

2.6. *Panchromatic Spectrum Assembly*
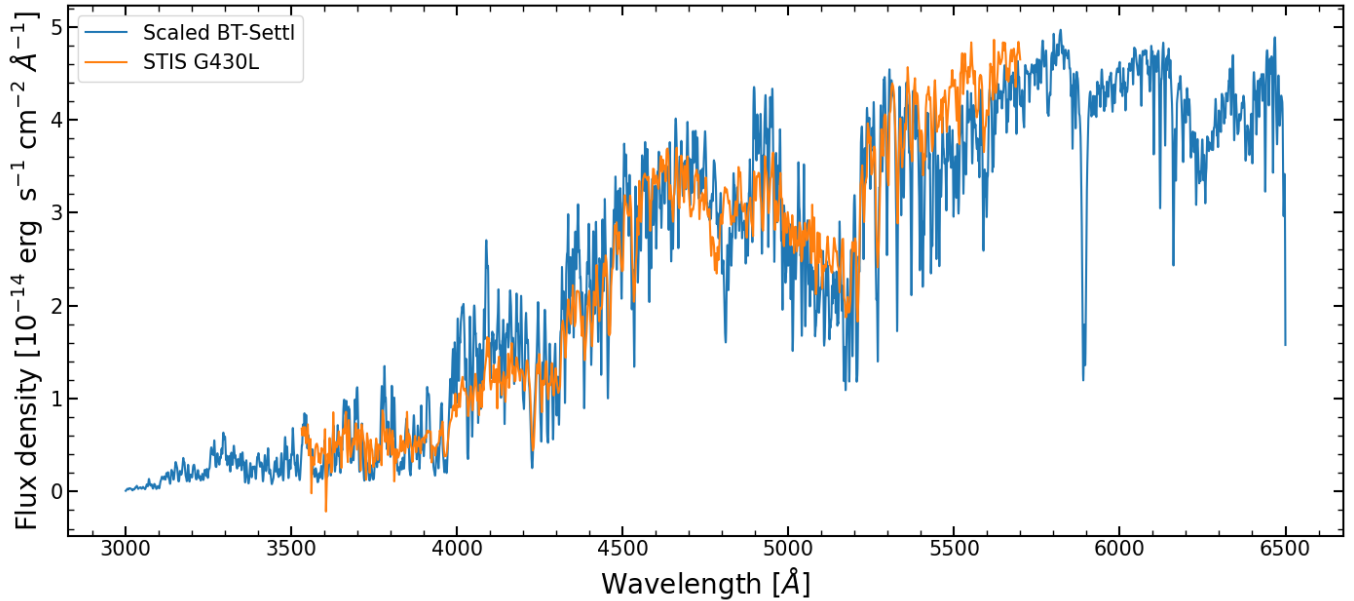
Figure 2: Result of the WASP-43 BT-Settl scaling routine plotted with the STIS G430L spectrum. The BT-Settl stellar atmosphere model is convolved to G430L resolution and scaled by a factor of 0.9210.

With all of the data products described above in hand we developed a procedure for stitching the spectra together into a continuous panchromatic spectrum. We first define a prioritization order for the spectral segments, placing the most priority on direct observations with good S/N, followed by Lyman-α reconstructions, and finally scaled proxy and BT-Settl spectra. We prioritized our own Lyman-α reconstructions over the scaled proxy spectra because the EUV portion of our proxy spectra are themselves estimations and thus it is more accurate to use the reconstructions based on our direct G140M and G230L observations.

Due to very low X-ray photon counts we were unable to create either differential emission measures (DEMs) or APEC models of the stellar X-ray spectra. We use the scaled proxy spectra in these regions as well, noting that the X-ray spectra for MUSCLES targets are a combinations of *Chandra* observations, *XMM-Newton* observations, and APEC plasma models with plasma temperatures ranging from $kT = 0.09 - 0.8$keV (see table 1 of Loyd et al. 2016). The total wavelength range spanned by scaled proxy spectra begins at 5Å and extends to anywhere from 1750Å (WASP-17) to 2600Å (LP 791-18), excluding the reconstructed Lyman-α range between $\sim 1212 - 1220$Å. The large spread in the red end of the proxy region is related to the effective temperature of the target star. By Wiens law, $\lambda_{peak} \propto 1/T_{eff}$, so increases in effective temperature drive the photospheric emission into shorter wavelengths, decreasing the red end of the proxy range compared to cooler stars (see figure 5).

Keeping in mind our goal of using direct observations wherever possible, we opted not to perform any optimization routine to determine the location of the joint. Instead, we directly inserted whichever data product was highest on the priority list for the given wavelength range. This occasionally results in a small jump discontinuity at the joining location but we find that the effect of these jumps are negligible. In cases where two direct observations overlap, we give priority to whichever observation has higher S/N over the region in question.

Figure 3 shows an example of the final panchromatic spectrum of the M dwarf L 98-59. The X-ray and UV ($5-2600$Å for this target) flux is estimated from the scaled proxy, GJ 832, from the MUSCLES survey.

The MUSCLES Extension SEDs will be available as high-level science products on the MAST archive as a FITS file containing a PrimaryHDU with general observation information and a BinTableHDU containing the spectral data. We provide two versions of each SED: one which retains the native instrument or model resolutions, and one which is rebinned to a constant 1Å resolution. Each panchromatic SED provides the following information:

- Bin: Midpoint and edges of the wavelength bins. For our unbinned spectra we report only the midpoint of the wavelength bin from the original data source
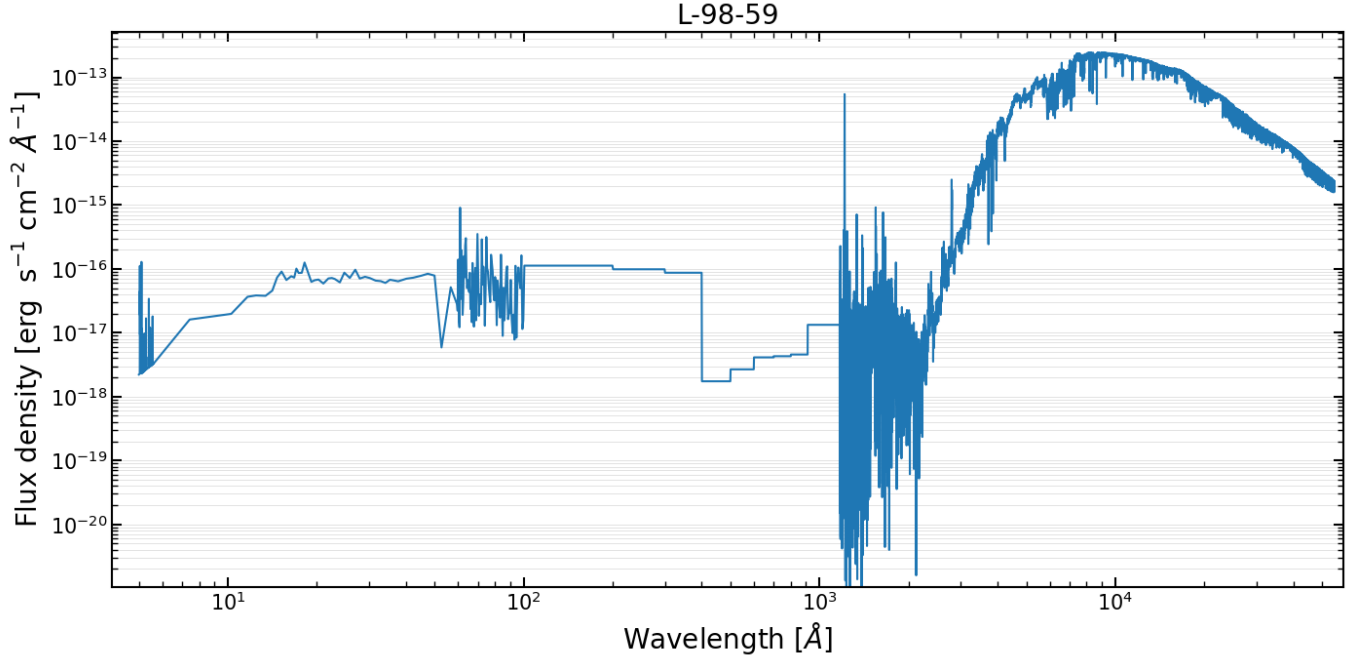
Figure 3: L 98-59 panchromatic spectrum from 5Å-5.5μm.

- Flux density: Measurement and error of the flux density in [erg s^{-1} cm^{-2} Å^{-1}] as well as the value normalized by the bolometric flux [Å^{-1}]

- Exposure: MJD of the beginning and end of the exposure as well the cumultive exposure time [s]

- Normalization: any normalization factor applied to flux bin

- Instrument: a bit-wise flag identifying the source of the flux data for the bin. Note that for binned spectra, we may have combined adjacent bins from different sources. This is accounted for in the bit-wise instrument flag by adding the bit value for each of the respective instruments.

3. RESULTS

France et al. (2018) showed that exoplanet hosting stars selected from RV and transit methods exhibit lower activity than general field stars which were not selectively chosen as planet hosts. We present a comparison of our targets to previously studied exoplanet hosting and non-exoplanet hosting stars in order to further understand the potential effects of selecting stars chosen from planet detection surveys to use as templates for atmospheric modeling. We examine first the fractional X-ray luminosity (Section 3.1), which may be considered an indicator of coronal activity levels, then the FUV/NUV flux ratio and fractional UV emission line luminosities (Sections 3.2 and 3.3), which we consider to be indicative of chromospheric/transition-region activity levels, and finally the UV flux environment experienced by the planets orbiting our target stars compared to those in the MUSCLES survey (Section 3.4). The X-ray flaring events of L 98-59 are discussed in Section 3.5.

3.1. X-ray flux

The fraction of stellar bolometric flux emitted in the X-ray band has been shown to be correlated with chromospheric and coronal activity indicators such as rotation period, R'_{HK}, and $R_{H\alpha}$, and thus is a useful measure of stellar activity levels (Kostov et al. 2019b; Katsova & Livshits 2011; He et al. 2019; Linsky et al. 2020). Figure 4 shows the fractional X-ray luminosity of MUSCLES Extension stars compared to a large survey by Wright et al. (2011, 2018). Wright et al. (2011) observed 824 solar and late-type stars to study the relation between rotation period and stellar activity; they extended this survey in Wright et al. (2018) to include a sample of 19 fully convective M dwarfs.

For this work, we use the X-ray flux from PIMMS as described in section 2.2 and define the bolometric flux based on effective temperature:

$$F_{bol} = \sigma T_{eff}^4 (\frac{R_*}{d})^2 \tag{3}$$

Where σ is the Stefan-Boltzman constant, R_* the stellar radius, and d the stellar distance. Using this definition of bolometric flux allows for consistency between measurements of our own targets as well as to those of France et al. (2018), who use the same definition.

Young, rapidly rotating stars show a saturation at $\log L_x/L_{bol} \sim -3$, and older stars begin to show a sharp decline in fractional X-ray luminosity after reaching rotation periods of a few days (Wright et al. 2011; Astudillo-Defru et al. 2017). Here, we take "active" stars to be broadly defined as those with $-5 \lesssim \log L_x/L_{bol} \lesssim -3$ and "inactive" as those with $\log L_x/L_{bol} < -5$ (Linsky 2019, and references therein). Under this definition we find that 9 of the 13 stars from this work exhibit low fractional X-ray luminosities consistent with little coronal activity. X-ray luminosities or upper limits thereof can be found in Table 3 (*Chandra* targets) and Table 2 (*XMM-Newton* targets). Note that the X-ray flare of L 98-59, indicated by an orange X in figure 4, pushes the star into the active regime, highlighting the importance of taking into account stellar variability, as we shall discuss in section 3.5.
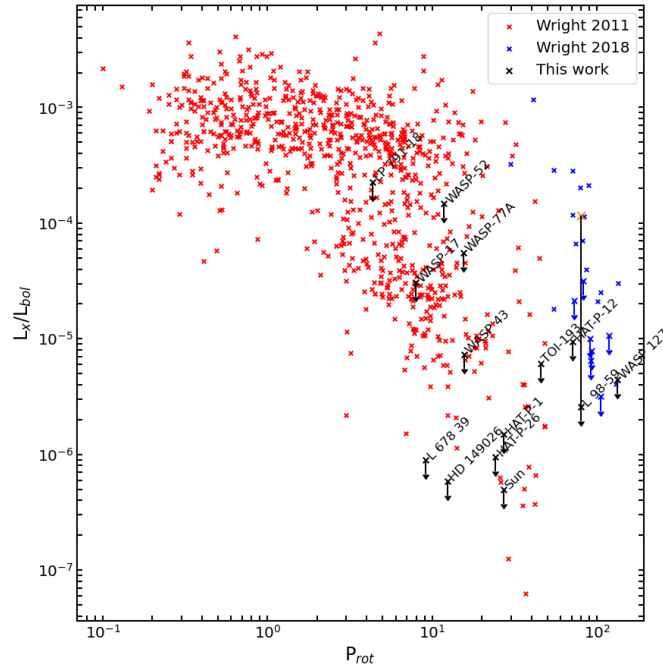
Figure 4: Fraction of bolometric luminosity emitted in the X-ray. Wright et al. (2011) represents solar and late-type stars. Wright et al. (2018) represents fully convective M dwarfs. The orange X connected by vertical line to L 98-59 represents the X-ray luminosity during only the flaring event. The black X representing L 98-59 shows the quiescent X-ray luminosity.

3.2. *FUV to NUV flux ratios*

The FUV to NUV flux ratio is an important measure for exoplanet habitability studies. As described in section 1.2, the FUV/NUV ratio impacts atmospheric oxygen chemistry via the Chapman reactions. FUV flux photolysizes CO_2 and O_2 leading to a buildup of atomic oxygen which may undergo three body recombination into O_2 and O_3. NUV flux may then photolysize O_3 and O_2 into atomic oxygen (Chapman 1930). However, for a star with a large FUV/NUV flux ratio, destruction of O_3 via NUV flux may not balance its creation from FUV flux, leading to an abiotic buildup of ozone and the detection of a potential false-alarm biosignature (Segura et al. 2010; Domagal-Goldman et al. 2014; Schwieterman et al. 2018).

While a larger fraction of the NUV is contributed by the stellar photosphere, the FUV/NUV ratio can also be thought of as a chromospheric activity indicator, as most of the stellar FUV flux from GKM stars comes from emission

lines as a result of stellar activity rather than continuum emission. It is important to keep in mind, however, that this ratio is strongly correlated with effective temperature. As T_{eff} increases, the photospheric emission of the star begins to push further into the NUV region, decreasing the FUV/NUV ratio. There is a minimum in the FUV/NUV ratio at $\sim 1M_\odot$ after the photospheric emission begins to push all the way into the FUV, resulting in an increase of FUV/NUV flux as shown in figure 5. This makes the FUV/NUV ratio less accurate as an activity indicator for hotter stars without subtracting the photospheric contribution. However, at a given stellar mass, the FUV/NUV ratio is a measure of the excess FUV emission contributed by chromospheric and transition region activity.
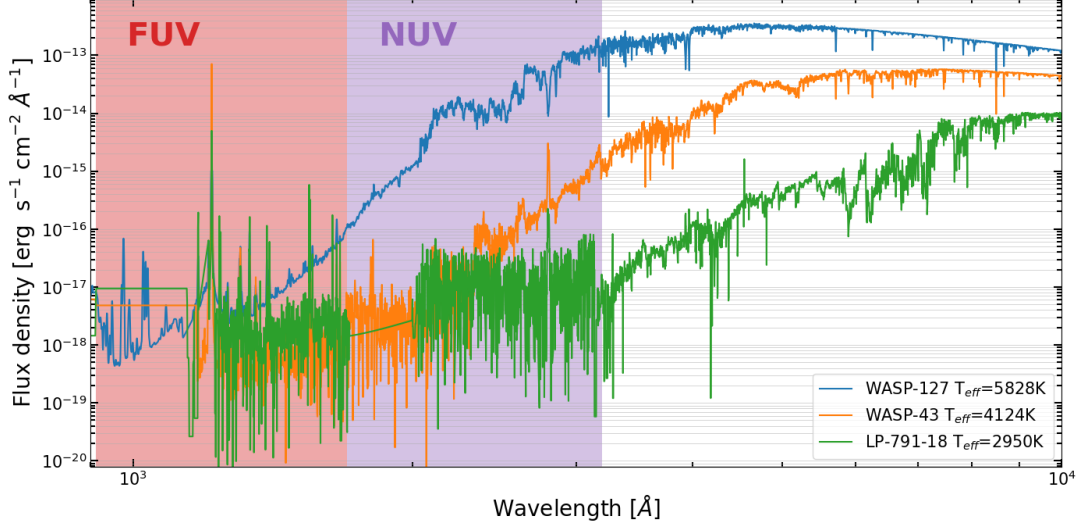
Figure 5: Stellar UV flux with increasing effective temperature. Note that increasing effective temperature drives the photospheric emission deeper into the UV as discussed in section 3.2

To put the MUSCLES Extension stars in context with the general stellar population, we compare them to the HAZMAT III (Schneider & Shkolnik 2018) and HAZMAT V (Richey-Yowell et al. 2019) surveys. Comparison to the HAZMAT study offers an opportunity to compare stars selectively chosen as exoplanet-hosts (MUSCLES Extension) to a non-selective field survey (HAZMAT). The HAZMAT III and HAZMAT V surveys present studies of 642 M-dwarfs and 455 K-dwarfs, respectively. Figure 6 shows the FUV/NUV flux ratio in the GALEX bandpass (FUV: 1350-1750Å, NUV: 1750-2800Å) of the MUSCLES Extension stars compared to a representative sample of stars from the two HAZMAT surveys. We performed a linear fit using a least-squares routine to fit the stars between 0.2-0.85$M_\odot$. The bounds of the fit exclude stars in the saturated FUV/NUV regime of $\sim 2 \times 10^{-1}$ at $M < 0.2M_\odot$, as well as the MUSCLES Extension stars with spectral type of F or G, as the HAZMAT surveys include only M and K dwarfs. The slopes of the linear fits are consistent within the 1σ level—-2.543 ± 0.230 for HAZMAT stars and -2.357 ± 0.451 for MUSCLES Extension stars. However, the MUSCLES Extension stars are considerably less FUV luminous than the HAZMAT stars, offset in their FUV/NUV ratio by $\sim 3\sigma$, suggesting that the MUSCLES Extension targets have significantly less FUV activity than the average populations of K and M dwarfs in the field.

To investigate the statistical significance of the offset, we applied a 1-sided Wilcoxon-Mann-Whitney U test. The U test is a nonparametric test applicable to small sample sizes of $N \lesssim 20$. The null hypothsis of the U test is that the distribution underlying sample X (in this case the MUSCLES Extension stars) is the same as the distribution underlying sample Y (HAZMAT stars). The alternative hypothesis for the 1-sided U test is that the distribution of X is stochastically *less* than the distribution of Y (Wall & Jenkins 2003). The U test yielded $p = 0.016$ and thus we reject the null hypothesis, indicating that MUSCLES Extension stars come from a different population than the HAZMAT stars and have a systematically lower FUV/NUV flux ratio at the 95% confidence level.

3.3. *UV Ion ratios*

We quantify chromospheric/transition region activity via the UV activity level indicators, F_{ion}/F_{bol}, for C II (λ 1334.53 Å, λ 1335.66 Å), Si IV (λ 1393.75 Å, λ 1402.76 Å), and Mg II (λ 2795.55 Å, λ 2802.70 Å). Figure 7 shows the
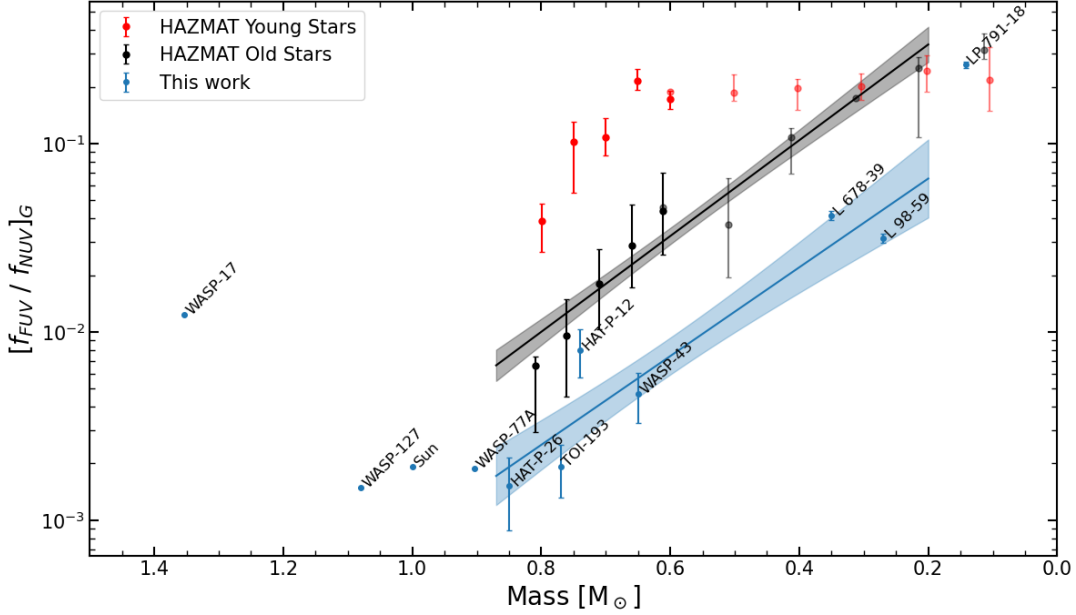
Figure 6: MUSCLES Extension stars compared with M and K dwarfs from the HAZMAT surveys. For stars from the HAZMAT surveys, transparent markers indicate M dwarfs from Schneider & Shkolnik (2018) while solid markers represent K dwarfs from Richey-Yowell et al. (2019). Shaded regions represent the 1σ error level of the linear fits.

MUSCLES Extension tagets plotted against both planet and non-planet hosting stars from the France et al. (2018) survey.

Here we apply both the Fisher exact test and the Wilcoxon-Mann-Whitney U to the Si IV flux measurements to test whether the stars come from the same population. The Fisher exact test looks for biomodality in two populations with the null hypothesis that the distribution is assigned randomly (Wall & Jenkins 2003). The two populations are the France et al. (2018) non-planet hosts and the MUSCLES Extension targets. We classify the potential bimodality as "active" stars with $L_{SiIV}/L_{bol} > 1 \times 10^{-6}$ and "inactive" stars with $L_{SiIV}/L_{bol} < 1 \times 10^{-6}$, as in France et al. (2018). The results from the exact test yielded a probability of obtaining the observed distribution of 0.07 and so we cannot say that the non-planet hosting and MUSCLES Extension targets represent two separate activity groups at the 95% confidence level.

Since the sample size is now larger ($N_1 + N_2 > 20$), the Wilcoxon-Mann-Whitney U statistic can be approximated as normally distributed with mean $\mu = m(N+1)/2$ and variance $\sigma^2 = mn(N+1)/12$, where m and n are the sample sizes of the two populations and $N = m + n$ (Wall & Jenkins 2003). Using only the non-planet hosting stars from France et al. (2018) and the MUSCLES Extension stars from this work, we find $U = 137$, corresponding to a value of 1.07σ above the mean under the normal approximation, suggesting that the non-planet hosting and MUSCLES Extension targets do come from distinct populations.

The conflicting results from the two tests applied to our observations are inconclusive and highlight the need for 1) further UV characterization of a larger number of exoplanet-hosting stars and 2) the use of multiple robust activity indicators when classifying a target as active or inactive.

3.4. *UV irradiation environment of exoplanets*

Absolute flux incident on the exoplanet atmosphere is critical for accurate atmospheric modeling (see discussion in Section 1). Here we present our FUV and NUV flux measurements in context of the closest orbiting planet for each system. Figure 8 shows the incident top-of-the-atmosphere FUV and NUV flux relative to the Earth/Sun system for the MUSCLES Extension targets and a subset of the original MUSCLES targets. Stars with a solar-like FUV/NUV ratio are those with little separation on the plot, while those with FUV/NUV ratios much different than the Sun (e.g., M dwarfs) have a large separation.

Many previous studies have used M dwarfs observed by the MUSCLES program as inputs to atmospheric models of hypothetical planets (e.g., Tian et al. (2014); Rugheimer et al. (2015); Chen et al. (2021)). This is the first

(a)

(b)
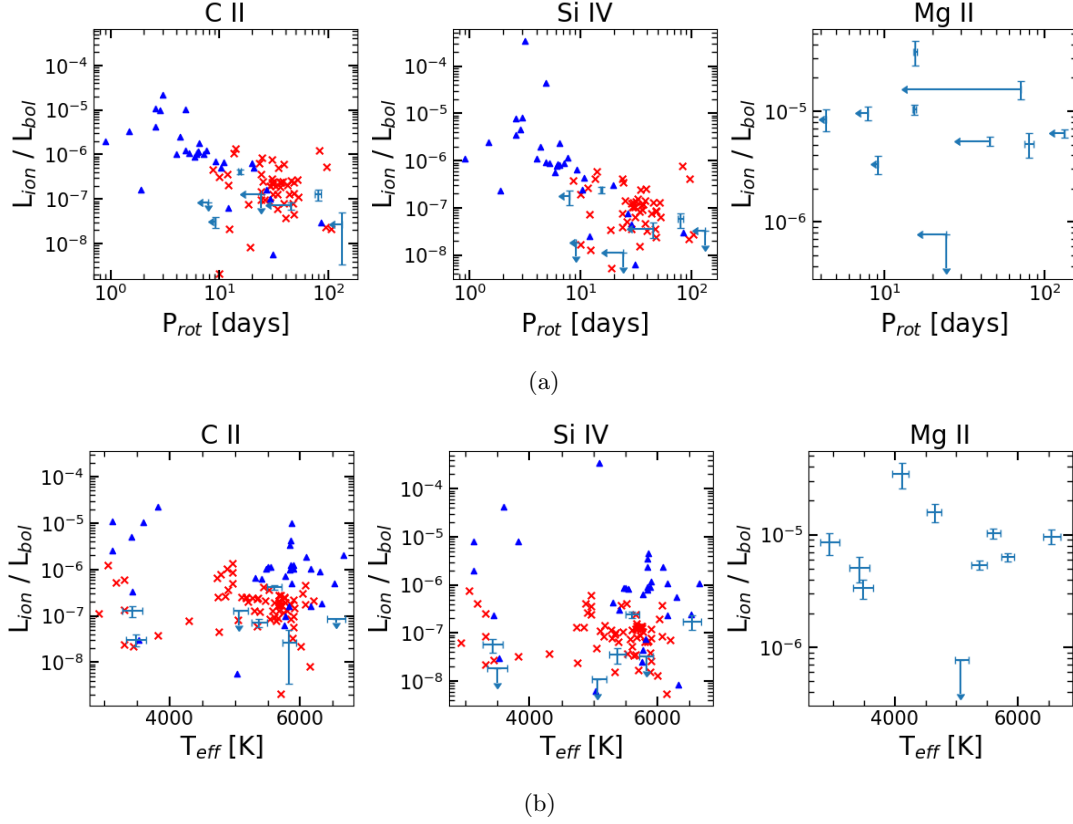
Figure 7: UV ion ratios vs (a) rotation period (b) effective temperature. × = France et al. (2018) non-planet hosts, ▲ = France et al. (2018) planet hosts, + = This work

time that FUV and NUV fluxes have been directly measured for an ensemble of stars whose planets have been or will be characterized with high-sensitivity spectrophometric observations, allowing for more accurate modeling of photochemical contributions to atmospheric composition and evolution.
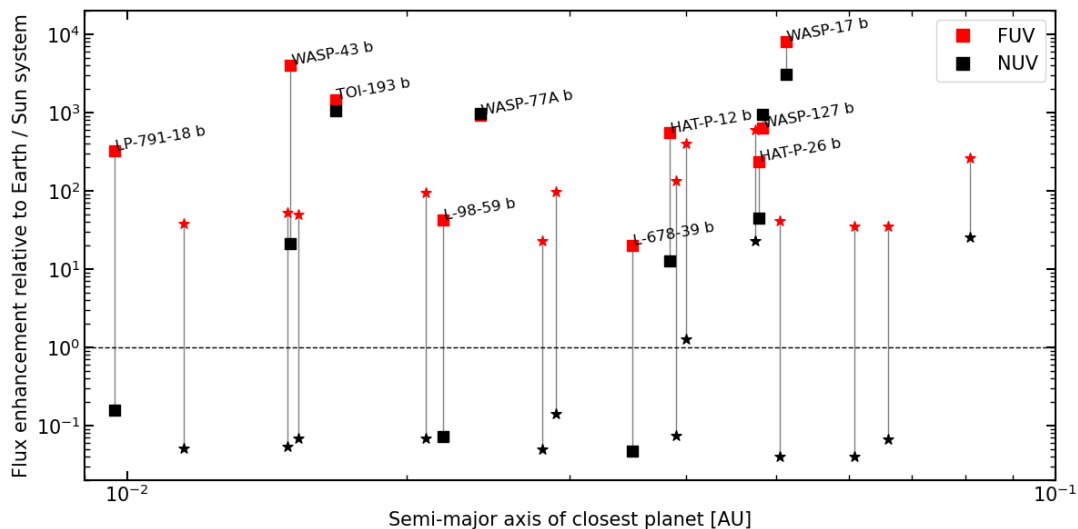
Planets around our G and F stars experience flux enhancements of $\sim 10^3 - 10^4$ relative to Earth/Sun in both the FUV and NUV, due to their smaller semi-major axes. Notably, the smaller M and K stars show FUV enhancements of $\sim 1-2$ orders of magnitude more that of the Earth/Sun but NUV decrements of ~ 1 order of magnitude *less* than the Earth/Sun system. This indicates a strong possibility of photochemical disequilibrium, as photodissociation rates in the FUV will be enhanced while those in the NUV, including O_3, will be suppressed relative to Earth. The influence of photochemical reactions on the composition of exoplanetary atmospheres will be empirically tested for the first time (e.g., *JWST* ERS team - in prep) by *JWST* in the next year.

3.5. *L 98-59 X-ray flare*

We obtained two *XMM-Newton* observations of L 98-59 which each had an X-ray flaring event. The first was on April 15, 2021 (obs.ID 0871800301, hereafter flare F301) and the second on April 16, 2021 (obs.ID 0871800201, hereafter flare F201). Both flares were detected in the EPIC pn and MOS detectors (X-ray; $\sim 0.3 - 10.0$ keV) and F301 was also detected in the Optical Monitor UV1 filter (OM UV1; 2000-4000Å). We extracted the light curves using the SAS *evselect* routine with a temporal bin size of 100s. The two flares are shown together, relative to the start time of their respective observations, in Figure 9. The background-subtracted count rates over the quiescent periods are $1.1 \pm 0.2 \times 10^{-2}$ s^{-1} for F301 and $8.4 \pm 2.6 \times 10^{-3}$ s^{-1} for F201. Defining the start time as the point where the light curve first exceeds the quiescent level, and the rise time as the difference between the time of peak count rate and the start time, we find that F301 began at 3300 ± 50 s and had a rise time of 400 ± 70 s. F201 began at 2900 ± 50 s into observation and had a longer rise time of 1000 ± 70 s.

L 98-59 does not return to its quiescent level during the length of the observation for either flare. However, we note that it does reach a level of constant count rate which is larger than that of the constant quiescent level. Thus, we are

Figure 8: FUV and NUV flux received by the closest planetary companion relative to the Earth/Sun system compared to MUSCLES survey. Squares markers (■) = This work. Star markers (⋆) = MUSCLES. The dashed horizontal line represents the same top-of-the-atmosphere flux as the Earth/Sun system. All planet labels are plotted at the location of their FUV data point.

unable to quantify a definitive duration. We report instead a lower limit duration which is the time from flare start to the end of the usable observation. The flare durations are > 15.7 ks for F301 and > 16.8 ks for F201. Because the durations are lower limits we report all values in the following subsections as lower limits as well.

Figure 9: Background subtracted X-ray light curves of L 98-59 during the flaring events, F301 and F201, from the EPIC pn detector. Temporal bin size is 100s for both observations.
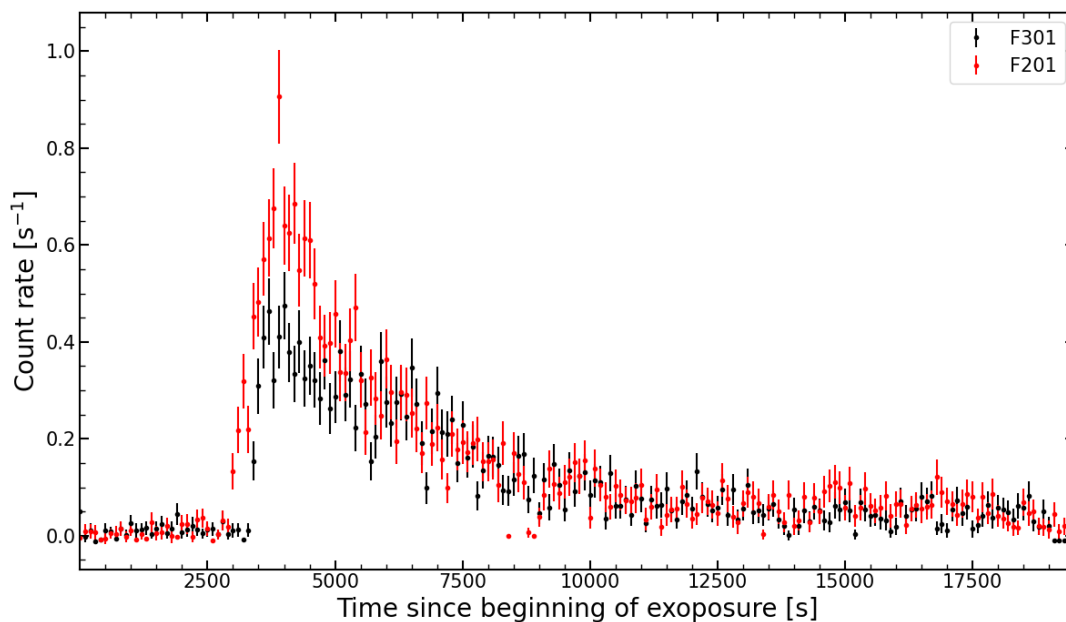
3.5.1. Flare luminosity and equivalent duration

We measured the flare luminosity by filtering the event list to include only events during the flare duration and converting the counts vs. instrument channel into flux vs. energy using the SAS *efluxer* routine. We then calculated the total luminosity by integrating the fluxed spectrum over the 0.3-10.0 keV band:

$$L_x = 4\pi d^2 \int F_f dE \tag{4}$$

where d is the stellar distance, and F_f the background subtracted flux in the energy band during the flare, and the integral is nominally taken over the entire flare duration. The calculated flare luminosities were $L_x > 2.38 \pm 0.31 \times 10^{27}$ erg s^{-1} for F301 and $L_x > 5.08 \pm 0.39 \times 10^{27}$ erg s^{-1} for F201. We then calculate the total energy released during the flare by multiplying the flare luminosity by the flare duration. The total flare energies were $E_x > 1.83 \pm 0.241 \times 10^{31}$ ergs for F301 and $E_x > 4.88 \pm 0.377 \times 10^{31}$ ergs for F201. In a recent study of Proxima Centauri, Fuhrmeister et al. (2022) find that during an average flare the ratio of peak count rate to quiescent count rate is 10 and the average flare luminosity is $L_x = 6.7 \times 10^{27}$ ergs s^{-1}. In comparison, we find larger peak to quiescent count rate ratios of 40 and 80 for F301 and F201 on L 98-59.

We also compute the equivalent duration, δ, of each flare. The equivalent duration represents the amount of time it would take the star, in the quiescent state, to release the same amount of energy as is released during the flare (Gershberg 1972; Hunt-Walker et al. 2012):

$$\delta = \int_{t_0}^{t_0+\Delta t} \frac{(R_f - R_q)}{R_q} dt \tag{5}$$

where t_0 is the start time of the flare, Δt the flare duration, R_f the 0.3-10keV count rate during the flare, and R_q the 0.3-10keV count rate during the quiescent period. The equivalent durations of the L 98-59 flares were $\delta > 130.4$ ks for F301 and $\delta > 245.9$ ks for F201. These are larger than the equivalent durations reported in Loyd et al. (2018) which had values $1.3 < \delta < 120.9$ ks for similarly inactive stars. However, the 2 of 3 flares from the MUSCLES study were also truncated before the end of the flare duration and thus the equivalent durations are likely similar to that of L 98-59.

Accounting for the flare increases L_x/L_{bol} to $> 45\times$ the upper limit quiescent level. This highlights the importance of accounting for high-energy flaring events in the XUV radiation environment of exoplanets around M dwarfs, especially as we have observed two similar events within a 24hr period.

3.5.2. *NUV flare*

The OM flare peaks during the rise time of the X-ray flare, shown in figure 10. Güdel et al. (2002) report a similar phenomenon during a flaring event of Proxima Centauri, for which they also obtained simultaneous *XMM-Newton* EPIC and OM observations. Güdel et al. (2002) propose a chromospheric evaporation scenario similar to the well-studied Neupert effect (Neupert 1968) in which a flaring event accelerates high-energy electrons into the chromosphere, where the subsequent deposition of energy causes a sharp optical signal and increase in chromospheric temperature driving hot plasma into the corona and resulting in the longer duration X-ray flare. The Neupert effect was first described in relation to simultaneous hard X-ray and microwave flares in the solar corona but had not been seen in the X-ray and NUV/optical prior to its observations on other stars. The X-ray/optical relation has since been observed in several stellar spectra of M and K dwarfs: in BY Draconis (K4) (de Jager et al. 1986), UV Ceti (M6) (de Jager et al. 1986; Schmitt et al. 1993), AD Leonis (M3) (Hawley et al. 1995), Proxima Centauri (M5.5) (Güdel et al. 2002, 2004), and now L 98-59 (M3). If the chromospheric evaporation scenario proposed by Güdel et al. (2002) is correct, one should expect the time derivative of the X-ray light curve to mimic the optical signal:

$$\frac{dL_x}{dt} \propto L_O \tag{6}$$

Figure 10 shows light curves from the EPIC and OM instruments during the F301 flaring event. We are not concerned with total counts in this analysis and as such we have rebinned both X-ray and NUV light curves to 10s intervals rather than 100s to obtain more accurate temporal measurements. As expected from eq (6), the time derivative of the X-ray lightcurve matches the shape of the OM light curve (Figure 10b), with a difference in peak timing of 27 ± 7s. This supports the theory of chromospheric evaporation occuring doing stellar flaring events.
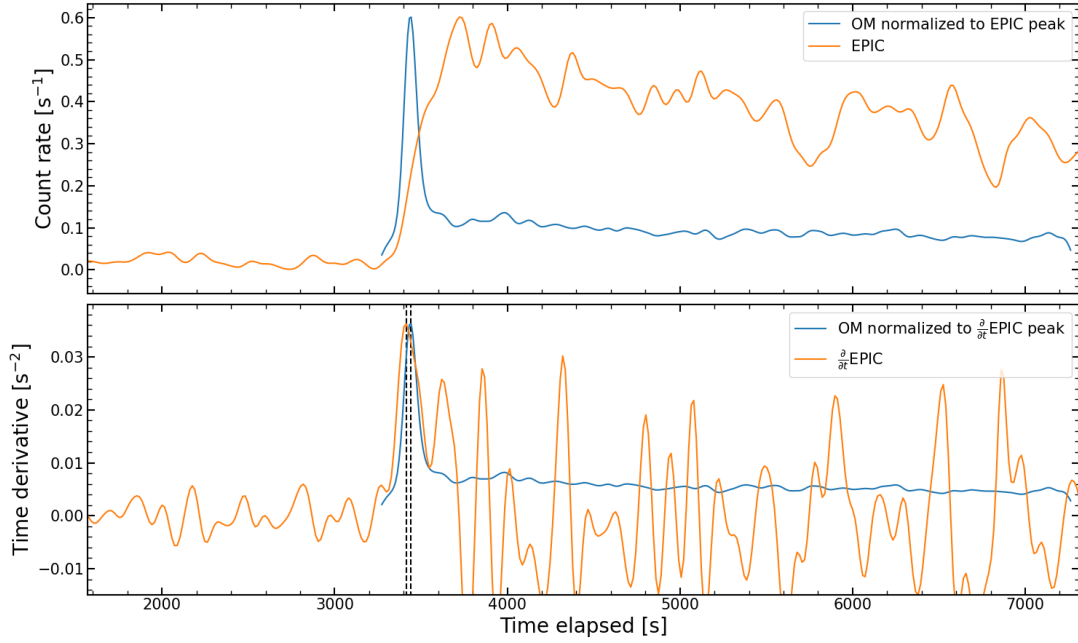
Figure 10: L 98-59 X-ray and optical light curves for F301. The EPIC light curves have been binned to 10s to match the time resolution of the OM data. The data have been smoothed with a Gaussian kernel for clarity. Top: OM flare normalized to the peak of the X-ray flare. Bottom: Time derivative of the X-ray flare (units of s^{-2}) overplotted by the normalized OM light curve (units of s^{-1}. Note that the blue OM curve does not match the units of the vertical axis and is only plotted here as a visual aid. The vertical black lines represent the location of the peak of each light curve.

4. SUMMARY

The MUSCLES Extension for Atmospheric Spectroscopy is an X-ray to IR survey of 13 confirmed exoplanet-hosting stars which have guaranteed *JWST* observing time yet no previous UV characterization. Of the 13 targets we provide panchromatic X-ray to IR SEDs for 11 stars.

We examine our targets on the basis of stellar activity levels by looking at the FUV/NUV flux ratio, the chromospheric and transition-region emission lines of C II λ1335Å, Si IV λ1400Å, and Mg II $\lambda\lambda$2796, 2803Å, and the fractional X-ray luminosity, L_x/L_{bol}, and place them in the context of the wider stellar population by comparing them to field surveys which were *not* selectively chosen as exoplanet hosting stars.

Magnetic processes are the main driver of activity in stars and drive the extreme heating of the stellar coronae which results in the emission of high-energy X-ray photons (Stepien & Ulmschneider 1989; Narain & Ulmschneider 1996; Pevtsov et al. 2003; Linsky 2019). High-energy X-ray radiation from host stars in turn drives ionization and heating in the upper atmosphere of exoplanets which can result in significant atmospheric escape (Lammer et al. 2007; Murray-Clay et al. 2009; Yelle et al. 2008). On the basis of fractional X-ray luminosity, we find that the majority of our observed targets (9 of 13) have low levels of fractional X-ray luminosity with $\log L_x/L_{bol} < -5$. This result is indicative of little coronal activity and is consistent with previous studies of these targets generally belonging to a population of inactive stars based on rotation periods and R'_{HK} measurements (see individual target descriptions in appendix A).

FUV and NUV radiation from host stars is a driver of atmospheric photochemistry and photochemical haze formation, which in turn impact the IR transmission spectra of their planetary companions (see sections 1.1,1.2). In our examination of the FUV/NUV flux ratios in section 3.2, we find that the MUSCLES Extension targets have a statistically lower flux ratio than even the oldest stars in the HAZMAT (Schneider & Shkolnik 2018; Richey-Yowell et al. 2019) surveys, indicating very low chromospheric activity levels and ages $\gtrsim$ 5Gyr. Our measurements of FUV ion ratios, L_{ion}/L_{bol}, for chromospheric and transition region emission lines show the expected decrease with stellar rotation period (a proxy for stellar age) and appear to be clustered with the low-activity stars from France et al. (2018), with our targets generally showing lower ion ratios than non-planet hosting stars of the same effective temper-

ature. However, our statistical analysis of this result was inconclusive; we suggest that UV emission measurements of additional exoplanet-hosting stars be made to investigate this hypothesis.

Finally, we examine the FUV and NUV flux experienced by our targets' planetary companions compared to the flux experienced by Earth. Our G and F stars show enhancement factors of $10^3 - 10^4$, consistent with their much smaller semi-major axes, and a small spread in the FUV and NUV enhancements, as expected from the pile-up around the solar FUV/NUV value from figure 6. Our M dwarf targets are consistent with those from the MUSCLES survey (France et al. 2016) and show less enhancement than expected from the $1/d^2$ relation of their closer semi-major axes, indicative of lower overall UV flux. The large difference in the FUV and NUV enhancements, with FUV being $\sim 10 - 100\times$ more than Earth and NUV being $\sim 10\times$ less, highlights the wide range of FUV/NUV ratios in.

Overall, we find that our targets are, in general, consistent with a population of particularly old and inactive stars. This is of particular importance in characterizing exoplanet atmospheres as the lifetime UV irradiation experienced by the planets is a critical driver of atmospheric composition and evolution.

The main results of this work are:

1. We have assembled panchromatic spectra from $5 - 5.5\mu m$ of 11 exoplanet hosting stars with guaranteed *JWST* observation time but no prior UV characterization with *HST*. The SEDs will be available as high-level science products on the MAST website and can be used as inputs for the stellar irradiance when modeling planetary atmospheres observed by *JWST*, eliminating the need to rely on optical scaling relations or stellar models without a complete treatment of the upper stellar atmospheres.

2. The planet-hosting stars from our survey follow the trend of France et al. (2018), displaying stastically lower activity levels than non-planet hosting groups on the basis of fractional X-ray luminosity and FUV/NUV flux ratios. This can easily be explained by a sample bias: confirmed exoplanets from RV and transit surveys largely (and in some cases intentionally (see refs in France et al. (2018)) select for low-activity stars, as active stars add excess noise to RV and transit measurements. However, as planet population estimates expect to find exoplanets around the vast majority of stars, selecting stellar irradiance levels based on samples of known exoplanet-host stars likely underestimates the UV flux experienced over a planet's lifetime and are not indicative of the radiation environments of the exoplanet population at large. Therefore, we present a cautionary speculation that the UV-driven atmospheric photochemistry on the average galactic exoplanet may be significantly different than what we measure on the current set of planets being studied by *JWST*.

3. We find a large X-ray flare on the M dwarf L 98-59 which increased the X-ray fraction of its bolometric flux by a factor of $> 45\times$ over quiescent levels. Depending on the frequency of flaring events, this could significantly increase the total amount of XUV irradiation of the planets orbiting this otherwise inactive star. This highlights the importance of studying time variability in exoplanet-hosting stars in order to accurately model a planet's lifetime-integrated UV irradiance.

Facilities: HST(STIS), XMM-Newton, Chandra(ACIS)

Software: astropy (Astropy Collaboration et al. 2013, 2018), scipy (Virtanen et al. 2020), matplotlib (Hunter 2007), SAOImage DS9 (Smithsonian Astrophysical Observatory 2000), Scientific Analysis System (Gabriel et al. 2004), CIAO (Fruscione et al. 2006)

APPENDIX

A. TARGETS

The targets for the MUSCLES Extension include 3 M dwarfs, 3 K dwarfs, 5 G type, and 1 F type stars. Notable differences from the original MUSCLES and Mega-MUSCLES survey are the inclusion of G and F type stars and the much larger distances to the targets. Our targets host a wide variety of exoplanets, from sub-Earth size through giant hot-Jupiters. This section is dedicated to providing a brief description of each planetary system as well as the spectral data used during construction of the SEDs.

A.1. *WASP-17*

WASP-17 is an F6 star at a distance of approximately 405pc (Gaia Collaboration et al. 2022). The star is estimated to have a rotation period of 8.5-11 days and an age of approximately 2.7Gyr with a sub-Solar metallicity of $[Fe/H] = -0.190 \pm 0.090$ (Bonomo et al. 2017). The system consists of one confirmed and peculiar exoplanet. WASP-17b is an ultra-low density planet with a radius of $R_p \approx 2R_J$ but a mass of only $M_p \approx 0.5M_J$. Initial observations of WASP-17b (Anderson et al. 2010) suggested the planet has a retrograde orbit; this was later confirmed by (Bayliss et al. 2010). The proposed explanation for WASP-17b's retrograde orbit is a combination of planet-planet scattering, the Kozai mechanism, and tidal circularization (Anderson et al. 2010, and references therein).

We obtained STIS G140L, G230L, and G430L observations of WASP-17. The G140L spectra showed no evidence of FUV emission line flux and had poor quality over the Lyman-α region. We did not obtain G140M spectra and therefore were unable to reconstruct the Lyman-α emission line using MCMC methods but the strong S/N in the NUV G230L observations allowed for estimation using the Mg II relation.

We obtain 23.84ks of new *Chandra* ACIS-S observations (obs.ID 201354, PI France) of WASP-17. Our X-ray analysis of the target was a non-detection and we present the 3σ upper for our further X-ray analysis as discussed in section 2.2.

The proxy star used for the XUV spectrum was Procyon, an F5 star with $T_{eff} \approx 7740K$. We obtained a high resolution UV spectrum of Procyon from the SISTINE II sounding rocket observation (Cruz-Aguirre et al. - in prep). The effective temperature of Procyon is $\sim 1200K$ higher than WASP-17 but we find that the NUV scaling procedure matched the shape of the spectrum very well in the G230L region from 1750-3150Å and we find that Procyon has $L_x/L_{bol} \sim 1 \times 10^{-5}$, similar to that of WASP-17, for which we find an upper limit of $L_x/L_{bol} \lesssim 3 \times 10^{-5}$. Thus, we believe that Procyon is a suitable proxy star for the XUV spectrum of WASP-17.

A.2. *HD-149026*

HD-149026 is a G0 star at a distance of approximately 76pc (Gaia Collaboration et al. 2022) with a super-Solar metallicty, $[Fe/H]=0.36 \pm 0.05$, and a single confirmed exoplanet with an unusually dense core (Sato et al. 2005). The exoplanet, HD 149026b, has a radius of $R = 0.725 \pm 0.05R_J$ but a density of 1.7 times that of Saturn. The high metallicity of the system in conjunction with the large density of the planet indicate that it may have an icy/rocky core that makes up 50-80% of the planetary mass (Sato et al. 2005; Fortney et al. 2006).

We obtained two G140M observations of HD-149026. The second observation had a misplaced extraction box during the X1DCORR routine and had to be re-extracted. After re-extraction we found the S/N of the G140M observations to be sufficient to reconstruct the Lyman-α emission line.

We retrieved 10.8ks of archival *XMM-Newton* observations (obs.ID 0763460301, PI Salz) in which we detect the target. King et al. (2018) report a soft X-ray (0.2-2.4keV) luminosity at earth of $\log L_x = 27.77$ erg s^{-1}, which we adopt for the X-ray analysis in this work.

While we suggest that the spectrum of the quiet Sun may be a suitable XUV proxy for HD-149026, we were unable to scale the spectrum to the observed E230M data and therefore do not present a panchromatic spectrum for this target. We opt to still include it in the survey as we were able to obtain useful G140M data and *XMM-Newton* X-ray data and report the L_{SiII}/L_{bol} and L_x/L_{bol} values as activity indicators.

A.3. *WASP-127*

WASP-127 is a G5 star with an estimated age of approximately 11Gyr (Lam et al. 2017). Gaia DR3 2022 parallax places the system at a distance of 160pc. Its planetary companion, WASP-127b, has an anomalously low density, with a sup-Saturn mass of $M = 0.18 \pm 0.02M_J$, super-Jupiter radius of $R = 1.37 \pm 0.04R_J$, and orbital period of 4.17 days, WASP-127b falls within the previously discussed sub-Neptune desert (Lam et al. 2017; Skaf et al. 2020). Transmission spectroscopy of WASP-127b shows a feature-rich spectrum including absorption by Na, H_2O, and either CO_2 or CO

Spake et al. (2021). Additionally, the low density "puffiness" of WASP-127b's atmosphere is unlikely to be caused by photo-evaporation due to its host star's low UV flux(Palle et al. 2017; Skaf et al. 2020) making it an interesting target for alternative atmospheric inflation processes (see Skaf et al. 2020, and references therein).

We obtained STIS G140L, G140M, G230L, and G430L observations of WASP-127. The FUV G140L spectrum showed no evidence of FUV emission lines and the Lyman-α emission from G140M was insufficient to recreate the intrinsic emission from MCMC methods so we opted to use the Mg II scaling relation. The NUV G230L spectrum breaks the S/N> 3 threshold for wavelengths of $\lambda > 2050$Å and extremely faint Mg II emission.

We retrieved 8ks of archival *XMM-Newton* observations (obs.ID 0853380601, PI Schartel) which yielded a non-detection of the target.

The XUV proxy for WASP-127 is the quiet solar spectrum (Woods et al. 2009). Despite its higher T$_{eff}$, we chose the solar spectrum based on its similarly low chromopsheric and coronal activity levels and find that it provides a good fit to the stellar continuum below ~ 2600Å.

A.4. *TOI-193*

TOI-193, also designated LTT 9779, is a solar-like main-sequence G7 star. It has an estimated age of 2Gyr and a super-solar metallicity of [Fe/H] $= 0.25 \pm 0.04$ (Jenkins et al. 2020). Gaia DR3 2022 parallax places the system at a distance of 81pc. Jenkins et al. (2020) confirmed an exoplanet, TOI-193b, with a mass of $M = 9.225^{+0.245}_{-0.255} \times 10^{-2} M_J$, radius of $R = 0.421 \pm 0.021 R_J$, and orbital period of 0.79d. Like WASP-127b, this places TOI-193b firmly within the Neptune desert, offering another opportunity to study the region between hot-Jupiters and super-Earths.

We obtained STIS G140L, G140M, G230L, and G430L observations of TOI-193. The G140L FUV observations did not show any emission lines above the S/N> 3 threshold. We detect Lyman-α emission in the G140M spectrum albeit with low S/N. Despite the quality we were able to reconstruct the Lyman-α emission line from G140M observations. The G230L NUV spectrum breaks the S/N threshold for wavelengths of $\lambda > 2200$Å and shows faint Mg II emission within the photospheric absorption band.

We also obtained a new 22.89ks *Chandra* ACIS-S observation of TOI-193 which showed a non-detection.

The XUV proxy star chosen was again the quiet solar spectrum based on similar UV activity level indicators.

A.5. *WASP-77A*

WASP-77A is a G8 star with a K-dwarf companion. Maxted et al. (2013) report WASP-77A to be solar-like in mass, radius, and metallicity; follow-up observations by Cortés-Zuleta et al. (2020) yield a slightly sub-solar metallicity of [Fe/H] $= -0.10^{+0.10}_{-0.11}$. Maxted et al. (2013) report an age of ~ 1Gyr using a rotation period relation or an age of ~ 8Gyr using stellar models. Following studies (Cortés-Zuleta et al. 2020; Bonomo et al. 2017) report an age of ~ 6Gyr and a $\log R'_{HK} = -4.57 \pm 0.02$ (Salz et al. 2015), indicating a low activity, sub-Solar star. The single confirmed exoplanet, WASP-77Ab, is a typical hot-Jupiter with $M = 1.76 \pm 0.06 M_J$, $R = 1.21 \pm 0.02 R_J$, and period of 1.36d (Maxted et al. 2013). It is estimated to have a high mass-loss rate from previous X-ray studies (Salz et al. 2015) and provides a promising opportunity to study hot-Jupiter planets around solar-like stars.

We obtained STIS G140L, G140M, G230L, and G430L observations of WASP-77A. We find that the STIS FUV observations have S/N > 3 for most emission lines. However, despite good S/N in the emission lines, we were unable to reconstruct the Lyman-α line using the MCMC method and so report the estimated flux based on the Mg II relation. The G230L NUV observations break the S/N> 3 threshold for wavelengths of $\lambda > 2000$Å and show Mg II in emission within the photospheric absorption band.

We retrieved 9.94ks of *Chandra* ACIS-S observations (obs.ID 15709, PI Salz). Salz et al. (2015) detect the target in their observation and provide a soft X-ray (0.2-2.0keV) luminosity of $\log L_x = 28.15$ erg s^{-1}. We opted for a larger energy band (0.3-10.0keV, as discussed in section 2.2) and find a larger X-ray luminosity, yielding an upper limit on the fractional X-ray luminosity of $\log L_x/L_{bol} = -4.25$.

The XUV proxy star was again the quiet solar spectrum based on similar UV activity level indicators.

A.6. *HAT-P-26*

HAT-P-26 is a K1 star at a distance of 142pc (Gaia Collaboration et al. 2022). Initial observations (Hartman et al. 2011) reported the star to be slightly smaller than the Sun with a similar metallicity of [Fe/H] $= -0.04 \pm 0.08$. The system has an age of $9.0^{+3.0}_{-4.9}$Gyr and $\log R'_{HK} = -4.992$ (Hartman et al. 2011); this indicates that HAT-P-26 is an old and inactive star. The exoplanet, HAT-P-26b, is a Neptune-sized planet with $M = 0.059 \pm 0.007 M_J$,

$R = 0.565^{+0.072}_{-0.032} R_J$, and period of 4.23d (Hartman et al. 2011), making it the third star from this study which falls in the Neptune desert. It is notable for its low density which is consistent with an irradiated planet with $10 M_\oplus$ rocky core and $8 M_\oplus$ gas envelope (Hartman et al. 2011, based on Fortney et al. (2007)). Hartman et al. (2011) suggest that HAT-P-26b may have started its life as a Jupiter sized planet and lost $\sim 30\%$ of its initial mass based on the energy-limited escape described by Erkaev et al. (2007) and Yelle et al. (2008). However, Hartman et al. (2011) note that due to the lack of knowledge of the XUV flux of its host star, the exact value of HAT-P-26b's mass loss is poorly constrained.

We obtained STIS observations with the G140L, G140M, G230L, and G430L gratings. We find no evidence of UV emission lines other than Lyman-α in either the G140L or G140M observations. We also find no evidence of Mg II emission despite having good S/N beyond 2550Å in the G230L observation. This is consistent with Hartman et al. (2011)'s claim of HAT-P-26 being an inactive star. We report an upper limit Lyman-α flux based on the RMS value of the background subtracted region over the Mg II line.

We retrieved 17ks of archival **?** observations (obs.ID 0804790101, PI Sanz-Forcada). Our analysis of the observation showed a non-detection.

The XUV proxy for HAT-P-26 is HD 40307, a K2.5 dwarf observed during the MUSCLES survey. The G230L scaling routine provided a good fit to the shape of the spectrum with $\chi^2/\nu = 1.78$; however, we note that HD 40307 is a younger, more active star with strong Mg II and other FUV emission line fluxes and therefore we suggest that while the continuum is comparable, any researcher using the HAT-P-26 SED should refer to the upper limits listed in Table 4 for emission line fluxes.

A.7. *HAT-P-12*

HAT-P-12 is a K4 dwarf with a sub-solar metallicity of [Fe/H] $= -0.29 \pm 0.05$. Gaia DR3 2022 parallax places the system at a distance of 142pc. The single confirmed exoplanet, HAT-P-12b, first reported by (Hartman et al. 2009), is a low density gas giant with mass $M_p = 0.211 \pm 0.012 M_J$ and radius $R_p = 0.959^{+0.029}_{-0.021} R_J$, with an orbital period of 3.21d. HAT-P-12b is found to be consistent with models of an irradiated planet with a $\lesssim 10 M_\oplus$ rocky core and a H/He dominated gas envelope (Hartman et al. 2009, and references therein).

We obtained no G140L or G140M observations of HAT-P-12 and therefore cannot report any FUV emission line fluxes. However, we obtained both G230L and G430L observations with good S/N for wavelengths $\lambda > 2500$Å and were able to recreate the Lyman-α emission line based on the Mg II relation.

We retrieved 10ks of archival *XMM-Newton* observations (obs.ID 0853380901, PI Schartel). Our analysis of the observation showed a non-detection.

The XUV proxy for HAT-P-12 is HD 85512, a K6 dwarf observed in the MUSCLES survey. The Mg II emission of the scaled HD 85512 spectrum was $\sim 2\times$ larger than that of the HAT-P-12 emission, suggesting that the chromospheric UV emission line fluxes of the scaled proxy spectrum may be accurate within an order of magnitude.

A.8. *WASP-43*

WASP-43 is a K7 star with a DR3 parallax distance of ~ 87pc (Hellier et al. 2011; Gillon et al. 2012). The exoplanet, WASP-43b, was first reported by Hellier et al. (2011) as a hot-Jupiter with mass and radius $M_p = 2.0 \pm 0.1 M_J$ and $R_p = 1.06 \pm 0.05 R_J$, respectively, orbiting very close to the host star with a semi-major axis of 0.014AU and period of 0.813d. Follow-up observations using TRAPPIST by Gillon et al. (2012) confirmed these parameters with higher precision. Based on stellar rotation period, WASP-43 is estimated to be a young star around 0.4Gyr (Hellier et al. 2011); however, using the Fortney et al. (2010) relation between radius and age for a low-irradiation planet, Gillon et al. (2012) claim that WASP-43b is consistent with a much older planet. This discrepancy is also noted by Husnoo et al. (2012) and may potentially be explained by tidal interactions between the large planet and low-mass star leading to an increased stellar rotation rate and therefore an artificially younger age based on age-period relations (Pont 2009; Poppenhaeger & Wolk 2014; Brown et al. 2011). The results from our own stellar activity analysis show that WASP-43 is consistent with the population of old (~ 5Gyr) inactive stars.

Due to large distance and expected low activity, we obtained no FUV observations of WASP-43 with the G140L or G140M gratings. We obtained NUV spectra with G230L and G430L with S/N above the threshold for wavelengths of $\lambda > 2600$Å, including a strong Mg II emission line.

We obtained 28ks of *XMM-Newton* observations (obs.ID 0871800101, PI France) of WASP-43. The target was detected on the EPIC pn detector and U band Optical Monitor (OM) and we find no evidence of flaring activity.

The XUV proxy was HD 85512 which again provided a good continuum fit but we find the Mg II flux of the scaled proxy to be $\sim 0.5\times$ that of the WASP-43 emission, suggesting that UV emission lines of the scaled proxy may be slightly under-estimated.

A.9. *L 678-39*

L 678-39 (GJ 357, TOI-562) is a M2.5 star with a sub-Solar to Solar metallicity of [Fe/H] $= -0.12 \pm 0.16$ (Schweitzer et al. 2019). Gaia DR3 2022 parallax puts the system at a distance of approximately 9pc. Long stellar rotation period, low $\log R'_{HK}$ value of -5.37, and low X-ray flux place the host star in a regime of old age and low activity (Luque et al. 2019; Modirrousta-Galian et al. 2020). The L 678-39 system contains of 3 confirmed exoplanets consisting of one Earth-sized planet and two super-Earth planets (Luque et al. 2019). The Earth-sized planet L 678-39b (GJ 357b) has a mass of $M_p = 1.84 \pm 0.31 M_\oplus$ and radius $R_p = 1.217^{+0.084}_{-0.083} R_\oplus$ and is the closest to the host star at a distance of $a_p = 0.035 \pm 0.002 \mathrm{AU}$ and an orbital period of 3.93d. This system, along with the other two M dwarf systems in our study, is of interest due to the ongoing debate regarding the habitability of Earth-like planets around M dwarf stars.

We obtained FUV observations with the COS G130M and G160M gratings as well as STIS G140M for the Lyman-α emission. The high spectral resolution of the COS gratings provided good S/N over the FUV emission regions and we find a strong Lyman-α emission and reconstruct the intrinsic profile using the MCMC method of section 2.3. The NUV spectrum was obtained with STIS G230L and G430L and breaches the S/N> 3 threshold for wavelengths of $\lambda > 2600$Å. We detect a significant Mg II emission in the G230L spectrum.

We obtained a 33ks archival *XMM-Newton* observation (obs.ID 0840841501, PI Stelzer) in which L 678-39 was detected with the high sensitivity EPIC pn detector and find no evidence of flaring activity. Modirrousta-Galian et al. (2020) used the same observation and performed an in-depth analysis of the X-ray emission, reporting a fractional X-ray luminosity of $\log L_x/L_{bol} = -6.05 \pm 0.09$. The Modirrousta-Galian et al. (2020) value is similar to but slightly larger than our value of $\log L_x/L_{bol} = -6.25$. We adopt their value for our further X-ray analysis due to their higher fidelity measurements.

The XUV proxy for L 678-39 is GJ 832, an M1.5 dwarf observed in the MUSCLES survey. Again we find that the scaled proxy matches the continuum shape well ($\chi^2/\nu = 1.54$) but underestimates the Mg II emission.

A.10. *L 98-59*

L 98-59 (TOI-175) is a M3 dwarf with a metallicity of [Fe/H] $= -0.5 \pm 0.5$ (Kostov et al. 2019b; Cloutier et al. 2019). Cloutier et al. (2019) report $\log R'_{HK} = -5.4 \pm 0.11$. Combined with a rotational period of $p_{rot} \approx 78$d, this indicates an old, low-activity star (Astudillo-Defru et al. 2017).

The system consists of four confirmed Earth to sub-Neptune sized planets (L 98-59b,c,d Kostov et al. (2019b); L 98-59d Demangeon et al. (2021)) and has gained much interest in the few years since its original discovery, prompting several follow up studies and observation proposals (Howard et al. 2021; Barclay et al. 2021b; Pidhorodetska et al. 2021b; Cloutier et al. 2019). In this work we use the closest confirmed planet, L 98-59b, for our analysis. L 98-59b has a mass of $M_p = 0.4^{+0.16}_{-0.15} M_\oplus$ (Demangeon et al. 2021), radius of $R_p = 0.80 \pm 0.05 M_\oplus$, and period of 2.25d (Kostov et al. 2019b).

We obtained observations of L 98-59 with the STIS G140L, G140M, G230L, and G430L gratings. We find FUV emission lines greater than the S/N> 3 threshold in the G140L spectra and strong Lyman-α emission in the G140M observations. Thus, our FUV emission line fluxes are relatively well constrained and we were able to reconstruct the Lyman-α line using the MCMC method. Our measurements of the FUV emission line fluxes and X-ray luminosity are consistent with the previous findings of low chromospheric activity. The G230L NUV observations break the S/N threshold for wavelengths of $\lambda > 2600$Å

We obtained two new *XMM-Newton* observations (obs.ID 0871800201 and 0871800301, PI France) of duration 23ks and 29.1ks, respectively. The target was detected in both the EPIC pn and MOS detectors as well as the OM. Despite the target's low activity level indicators mentioned above, we find flaring events in both EPIC and OM detections which occur ~ 24hr apart. These flares are discussed in detail in section 3.5.

The XUV proxy star for L 98-59 is again GJ 832. Due to differences in spectral resolution, the Mg II emission cores of the scaled proxy spectrum are over-estimated relative to our G230L observations while the wings and region between the doublet is under-estimated. As we have strong S/N for nearly all of the UV emission lines for this target, the differences in the Mg II emission lines is a non-issue and the scaled proxy spectrum provides an excellent approximation of the continuum flux for L 98-59.

A.11. *LP 791-18*

LP 791-18 is an M6 dwarf with an approximately solar metallicity [Fe/H] $= -0.09 \pm 0.19$. Age estimates from $v \sin i$ provide a lower limit of > 5Gyr Crossfield et al. (2019). The star is host to two confirmed exoplanets: a super-Earth with $R_p = 1.1 R_\oplus$ and a sub-Neptune with $R_p = 2.3 R_\oplus$. The planets have assumed but unconfirmed masses of $2 M_\oplus$ and $7 M_\oplus$, respectively (Crossfield et al. 2019). Our analysis in this work uses only the closer-orbiting super-Earth, LP 791-18b. At the time of its discovery, this system was the third coolest confirmed exoplanet-hosting star—second to Teegarden's Star and TRAPPIST-1—making it of great interest to study the dynamics of multi-planet systems around small, very cool stars (Crossfield et al. 2019).

Due to the expected faintness of the target we obtained only NUV observations with the STIS G230L and G430L gratings. The G230L spectrum never breaks the S/N> 3 threshold except in the Mg II region which shows a faint emission line. The G430L spectrum did not break the S/N threshold until wavelengths of $\lambda > 3800$Å.

We obtained 23.79ks of new *Chandra* observation of LP 791-18 with the ACIS-S instrument (obs.ID 23320, PI France). Our analysis of the observation showed a non-detection.

The XUV proxy for LP 791-18 is Proxima Centauri (GJ 551), a ~ 5Gyr M5.5 dwarf observed in the MUSCLES survey. The scaled proxy spectrum matches the G230L continuum well despite the low S/N but the Mg II flux of Prox Cen is significantly larger than that of LP 791-18. The lower limit of LP 791-18's age and its apparent lack of activity suggest that the scaled proxy spectrum of Prox Cen may actually be representative of a much younger and more active star.

B. X-RAY AND UV FLUX MEASUREMENTS

Table 2: *XMM-Newton* Observations

Star	Obsid	Exposure time [ks]	Source Counts	Count rate [s^{-1}][a]	$F_x[ergs^{-1}cm^{-2}]$	$L_x[ergs^{-1}]$	L_x/L_{bol}
HAT-P-1	0853380801	4.9966	5	$< 1.801 \times 10^{-3}$	$< 3.13 \times 10^{-15}$	$< 9.59 \times 10^{27}$	$< 1.49 \times 10^{-6}$
HAT-P-12	0853380901	2.7875	4	$< 3.23 \times 10^{-3}$	$< 3.097 \times 10^{-15}$	$< 7.57 \times 10^{27}$	$< 9.45 \times 10^{-6}$
HAT-P-26	0804790101	14.041	14	9.97×10^{-4}	6.65×10^{-16}	1.60×10^{27}	9.57×10^{-7}
HD-149026	0763460301	10.816	37	2.25×10^{-3}	2.14×10^{-15}	5.90×10^{27}	5.85×10^{-7}
L 678-39	0840841501	22.409	93	3.17×10^{-3}	3.82×10^{-15}	3.70×10^{25}	5.28×10^{-7}
L 98-59	0871800301	3.0591	36	1.18×10^{-2}	$< 1.69 \times 10^{-15}$	$< 2.02 \times 10^{25}$	$< 4.62 \times 10^{-7}$
WASP-43	0871800101	24.761	119	3.80×10^{-3}	4.66×10^{-16}	4.22×10^{27}	7.36×10^{-6}
WASP-127	0853380601	1.0274	2	$< 8.76 \times 10^{-3}$	$< 1.12 \times 10^{-14}$	$< 3.44 \times 10^{28}$	$< 4.47 \times 10^{-6}$

[a] Upper limits represent the count rate required to produce a 3σ detection given the listed exposure time

Table 3: *Chandra* Observations[a]

Star	Obsid	Exposure time [ks]	Source Counts	Count rate [s^{-1}]	$F_x[ergs^{-1}cm^{-2}]$	$L_x[ergs^{-1}]$	L_x/L_{bol}
WASP-77A	15709	9.94	22	2.16×10^{-3}	1.19×10^{-13}	1.57×10^{29}	5.57×10^{-5}
WASP-17	23322	23.84	7	$< 3.78 \times 10^{-4}$	$< 2.39 \times 10^{-14}$	$< 4.81 \times 10^{29}$	$< 3.06 \times 10^{-5}$
LP 791-18	23320	23.79	5	$< 3.78 \times 10^{-4}$	$< 2.14 \times 10^{-14}$	$< 1.73 \times 10^{27}$	$< 2.27 \times 10^{-4}$
WASP-52	15728	9.84	12	1.12×10^{-3}	6.78×10^{-14}	2.51×10^{29}	1.48×10^{-4}
TOI-193	23321	22.89	3	$< 3.92 \times 10^{-4}$	$< 2.08 \times 10^{-14}$	$< 1.59 \times 10^{28}$	6.14×10^{-6}

[a] All *Chandra* observations were taken using the ACIS-S detector

Table 4. UV emission line flux measurements [ergs s^{-1} cm^{-2}]

Star	$F_{C\ III}$	$F_{Si\ III}$	$F_{N\ V}$	$F_{C\ II}$	$F_{Si\ IV}$	$F_{C\ IV}$	$F_{Mg\ II}$	$F_{Ly\alpha}$
WASP-17	$< 7.35 \times 10^{-17}$	—	$< 7.37 \times 10^{-17}$	$< 6.66 \times 10^{-17}$	$1.36 \pm 0.42 \times 10^{-16}$	$< 1.58 \times 10^{-16}$	$7.50 \pm 0.50 \times 10^{-15}$	2.85×10^{-15}
HD 149026	—	$1.43 \pm 0.17 \times 10^{-15}$	—	—	—	—	—	4.96×10^{-15}
WASP-127	$< 1.96 \times 10^{-16}$	$< 3.68 \times 10^{-15}$	$< 4.66 \times 10^{-17}$	$6.68 \pm 5.80 \times 10^{-17}$	$< 7.57 \times 10^{-17}$	$< 1.21 \times 10^{-16}$	$1.59 \pm 0.20 \times 10^{-14}$	7.41×10^{-15}
WASP-77A	$< 1.10 \times 10^{-16}$	$5.30 \pm 1.27 \times 10^{-16}$	$< 8.39 \times 10^{-17}$	$8.81 \pm 0.65 \times 10^{-16}$	$5.22 \pm 0.63 \times 10^{-16}$	$9.96 \pm 2.34 \times 10^{-16}$	$2.20 \pm 0.10 \times 10^{-14}$	5.09×10^{-15}
TOI-193	$< 2.05 \times 10^{-16}$	$< 5.16 \times 10^{-15}$	$< 6.76 \times 10^{-17}$	$2.41 \pm 0.41 \times 10^{-16}$	$1.21 \pm 0.41 \times 10^{-16}$	$< 1.27 \times 10^{-16}$	$1.81 \pm 0.21 \times 10^{-14}$	$< 2.87 \times 10^{-15}$
HAT-P-26	$< 1.52 \times 10^{-16}$	$< 4.18 \times 10^{-15}$	$< 4.55 \times 10^{-17}$	$< 7.58 \times 10^{-17}$	$< 5.38 \times 10^{-17}$	$< 9.58 \times 10^{-17}$	$< 4.62 \times 10^{-16}$	8.95×10^{-15}
HAT-P-12	—	—	—	—	—	—	$5.14 \pm 0.09 \times 10^{-15}$	3.31×10^{-14}
WASP-43	—	—	—	—	—	—	$2.18 \pm 0.02 \times 10^{-14}$	1.28×10^{-13}
L 678-39	$9.56 \pm 3.47 \times 10^{-17}$	$1.17 \pm 0.27 \times 10^{-16}$	$1.29 \pm 0.30 \times 10^{-16}$	$2.09 \pm 0.44 \times 10^{-16}$	$5.30 \pm 7.41 \times 10^{-17}$	$5.82 \pm 1.84 \times 10^{-16}$	$2.29 \pm 0.03 \times 10^{-14}$	9.50×10^{-14}
L 98-59	$< 2.00 \times 10^{-16}$	$< 2.40 \times 10^{-15}$	$3.68 \pm 0.52 \times 10^{-17}$	$4.73 \pm 0.50 \times 10^{-16}$	$2.09 \pm 0.46 \times 10^{-16}$	$1.42 \pm 0.13 \times 10^{-15}$	$1.84 \pm 0.02 \times 10^{-14}$	7.59×10^{-15}
LP 791-18	—	—	—	—	—	—	$1.72 \pm 0.07 \times 10^{-15}$	—

REFERENCES

Aarnio, A. N., Stassun, K. G., Hughes, W. J., & McGregor, S. L. 2011, SoPh, 268, 195, doi: 10.1007/s11207-010-9672-7

Airapetian, V. S., Glocer, A., Khazanov, G. V., et al. 2017, ApJL, 836, L3, doi: 10.3847/2041-8213/836/1/L3

Allard, F., Homeier, D., & Freytag, B. 2011, in Astronomical Society of the Pacific Conference Series, Vol. 448, 16th Cambridge Workshop on Cool Stars, Stellar Systems, and the Sun, ed. C. Johns-Krull, M. K. Browning, & A. A. West, 91. https://arxiv.org/abs/1011.5405

Anderson, D. R., Hellier, C., Gillon, M., et al. 2010, ApJ, 709, 159, doi: 10.1088/0004-637X/709/1/159

Arney, G. N., Meadows, V. S., Domagal-Goldman, S. D., et al. 2017, ApJ, 836, 49, doi: 10.3847/1538-4357/836/1/49

Astropy Collaboration, Robitaille, T. P., Tollerud, E. J., et al. 2013, A&A, 558, A33, doi: 10.1051/0004-6361/201322068

Astropy Collaboration, Price-Whelan, A. M., Sipőcz, B. M., et al. 2018, AJ, 156, 123, doi: 10.3847/1538-3881/aabc4f

Astudillo-Defru, N., Delfosse, X., Bonfils, X., et al. 2017, A&A, 600, A13, doi: 10.1051/0004-6361/201527078

Ballester, G. E., & Ben-Jaffel, L. 2015, ApJ, 804, 116, doi: 10.1088/0004-637X/804/2/116

Barclay, T., Brande, J., Colon, K., et al. 2021a, in American Astronomical Society Meeting Abstracts, Vol. 53, American Astronomical Society Meeting Abstracts, 302.08

Barclay, T., Brande, J., Colon, K., et al. 2021b, in American Astronomical Society Meeting Abstracts, Vol. 53, American Astronomical Society Meeting Abstracts, 302.08

Bayliss, D. D. R., Winn, J. N., Mardling, R. A., & Sackett, P. D. 2010, ApJL, 722, L224, doi: 10.1088/2041-8205/722/2/L224

Bean, J. L., Miller-Ricci Kempton, E., & Homeier, D. 2010, Nature, 468, 669, doi: 10.1038/nature09596

Bean, J. L., Stevenson, K. B., Batalha, N. M., et al. 2018, PASP, 130, 114402, doi: 10.1088/1538-3873/aadbf3

Berta, Z. K., Charbonneau, D., Désert, J.-M., et al. 2012, ApJ, 747, 35, doi: 10.1088/0004-637X/747/1/35

Bonomo, A. S., Desidera, S., Benatti, S., et al. 2017, A&A, 602, A107, doi: 10.1051/0004-6361/201629882

Brown, D. J. A., Collier Cameron, A., Hall, C., Hebb, L., & Smalley, B. 2011, MNRAS, 415, 605, doi: 10.1111/j.1365-2966.2011.18729.x

Bryson, S., Coughlin, J., Batalha, N. M., et al. 2020, AJ, 159, 279, doi: 10.3847/1538-3881/ab8a30

Burkholder, J. B., Sander, S., Abbatt, J., et al. 2015, Chemical Kinetics and Photochemical Data for Use in Atmospheric Studies, Evaluation No. 18, Tech. rep., Jet Propulsion Laboratory, Jet Propulsion Laboratory, Pasadena, CA

Burrows, A., & Orton, G. 2010, in Exoplanets, ed. S. Seager, 419–440

Chapman, S. 1930, Mem. Roy. Meteor., 3, 103

Chen, H., Zhan, Z., Youngblood, A., et al. 2021, Nature Astronomy, 5, 298, doi: 10.1038/s41550-020-01264-1

Cloutier, R., Astudillo-Defru, N., Bonfils, X., et al. 2019, A&A, 629, A111, doi: 10.1051/0004-6361/201935957

Cortés-Zuleta, P., Rojo, P., Wang, S., et al. 2020, A&A, 636, A98, doi: 10.1051/0004-6361/201936279

Crossfield, I. J. M., Waalkes, W., Newton, E. R., et al. 2019, ApJL, 883, L16, doi: 10.3847/2041-8213/ab3d30

de Jager, C., Heise, J., Avgoloupis, S., et al. 1986, A&A, 156, 95

Demangeon, O. D. S., Zapatero Osorio, M. R., Alibert, Y., et al. 2021, A&A, 653, A41, doi: 10.1051/0004-6361/202140728

Des Marais, D. J., Harwit, M. O., Jucks, K. W., et al. 2002, AsBio, 2, 153, doi: 10.1089/15311070260192246

Domagal-Goldman, S. D., Segura, A., Claire, M. W., Robinson, T. D., & Meadows, V. S. 2014, ApJ, 792, 90, doi: 10.1088/0004-637X/792/2/90

Dressing, C. D., & Charbonneau, D. 2015, ApJ, 807, 45, doi: 10.1088/0004-637X/807/1/45

Erkaev, N. V., Kulikov, Y. N., Lammer, H., et al. 2007, A&A, 472, 329, doi: 10.1051/0004-6361:20066929

Fortney, J. J., Baraffe, I., & Militzer, B. 2010, in Exoplanets, ed. S. Seager, 397–418

Fortney, J. J., Dawson, R. I., & Komacek, T. D. 2021, Journal of Geophysical Research (Planets), 126, e06629, doi: 10.1029/2020JE006629

Fortney, J. J., Marley, M. S., & Barnes, J. W. 2007, ApJ, 659, 1661, doi: 10.1086/512120

Fortney, J. J., Saumon, D., Marley, M. S., Lodders, K., & Freedman, R. S. 2006, ApJ, 642, 495, doi: 10.1086/500920

Fossati, L., Erkaev, N. V., Lammer, H., et al. 2017, A&A, 598, A90, doi: 10.1051/0004-6361/201629716

France, K., Arulanantham, N., Fossati, L., et al. 2018, ApJS, 239, 16, doi: 10.3847/1538-4365/aae1a3

France, K., Froning, C. S., Linsky, J. L., et al. 2013, ApJ, 763, 149, doi: 10.1088/0004-637X/763/2/149

France, K., Loyd, R. O. P., Youngblood, A., et al. 2016, ApJ, 820, 89, doi: 10.3847/0004-637X/820/2/89

France, K., Duvvuri, G., Egan, H., et al. 2020a, AJ, 160, 237, doi: 10.3847/1538-3881/abb465

—. 2020b, AJ, 160, 237, doi: 10.3847/1538-3881/abb465

France, K., Fleming, B., Youngblood, A., et al. 2022, Journal of Astronomical Telescopes, Instruments, and Systems, 8, 014006, doi: 10.1117/1.JATIS.8.1.014006

Fressin, F., Torres, G., Charbonneau, D., et al. 2013, ApJ, 766, 81, doi: 10.1088/0004-637X/766/2/81

Froning, C. S., Kowalski, A., France, K., et al. 2019, arXiv e-prints, arXiv:1901.08647. https://arxiv.org/abs/1901.08647

Fruscione, A., McDowell, J. C., Allen, G. E., et al. 2006, in Society of Photo-Optical Instrumentation Engineers (SPIE) Conference Series, Vol. 6270, Society of Photo-Optical Instrumentation Engineers (SPIE) Conference Series, ed. D. R. Silva & R. E. Doxsey, 62701V, doi: 10.1117/12.671760

Fu, G., Sing, D. K., Lothringer, J. D., et al. 2022, ApJL, 925, L3, doi: 10.3847/2041-8213/ac4968

Fuhrmeister, B., Zisik, A., Schneider, P. C., et al. 2022, A&A, 663, A119, doi: 10.1051/0004-6361/202243077

Gabriel, C., Denby, M., Fyfe, D. J., et al. 2004, in Astronomical Society of the Pacific Conference Series, Vol. 314, Astronomical Data Analysis Software and Systems (ADASS) XIII, ed. F. Ochsenbein, M. G. Allen, & D. Egret, 759

Gaia Collaboration, Vallenari, A., Brown, A. G. A., et al. 2022, arXiv e-prints, arXiv:2208.00211. https://arxiv.org/abs/2208.00211

Gao, P., Hu, R., Robinson, T. D., Li, C., & Yung, Y. L. 2015, ApJ, 806, 249, doi: 10.1088/0004-637X/806/2/249

Gershberg, R. E. 1972, Ap&SS, 19, 75, doi: 10.1007/BF00643168

Gillon, M., Triaud, A. H. M. J., Fortney, J. J., et al. 2012, A&A, 542, A4, doi: 10.1051/0004-6361/201218817

Güdel, M., Audard, M., Reale, F., Skinner, S. L., & Linsky, J. L. 2004, A&A, 416, 713, doi: 10.1051/0004-6361:20031471

Güdel, M., Audard, M., Skinner, S. L., & Horvath, M. I. 2002, ApJL, 580, L73, doi: 10.1086/345404

Hartman, J. D., Bakos, G. Á., Torres, G., et al. 2009, ApJ, 706, 785, doi: 10.1088/0004-637X/706/1/785

Hartman, J. D., Bakos, G. Á., Kipping, D. M., et al. 2011, ApJ, 728, 138, doi: 10.1088/0004-637X/728/2/138

Hawley, S. L., Fisher, G. H., Simon, T., et al. 1995, ApJ, 453, 464, doi: 10.1086/176408

He, C., Hörst, S. M., Lewis, N. K., et al. 2018, ApJL, 856, L3, doi: 10.3847/2041-8213/aab42b

He, L., Wang, S., Liu, J., et al. 2019, ApJ, 871, 193, doi: 10.3847/1538-4357/aaf8b7

Hellier, C., Anderson, D. R., Collier Cameron, A., et al. 2011, A&A, 535, L7, doi: 10.1051/0004-6361/201117081

Howard, W. S., Teske, J., Corbett, H., et al. 2021, AJ, 162, 147, doi: 10.3847/1538-3881/ac0fe3

Hu, R., Seager, S., & Bains, W. 2012, ApJ, 761, 166, doi: 10.1088/0004-637X/761/2/166

Hunt-Walker, N. M., Hilton, E. J., Kowalski, A. F., Hawley, S. L., & Matthews, J. M. 2012, PASP, 124, 545, doi: 10.1086/666495

Hunter, J. D. 2007, Computing in Science & Engineering, 9, 90, doi: 10.1109/MCSE.2007.55

Husnoo, N., Pont, F., Mazeh, T., et al. 2012, MNRAS, 422, 3151, doi: 10.1111/j.1365-2966.2012.20839.x

Jakosky, B. M., Grebowsky, J. M., Luhmann, J. G., et al. 2015, Science, 350, doi: 10.1126/science.aad0210

Jenkins, J. S., Díaz, M. R., Kurtovic, N. T., et al. 2020, Nature Astronomy, 4, 1148, doi: 10.1038/s41550-020-1142-z

Johnstone, C. P., Güdel, M., Stökl, A., et al. 2015, ApJL, 815, L12, doi: 10.1088/2041-8205/815/1/L12

Kaltenegger, L. 2017, ARA&A, 55, 433, doi: 10.1146/annurev-astro-082214-122238

Kasting, J. F., Whitmire, D. P., & Reynolds, R. T. 1993, Icarus, 101, 108, doi: 10.1006/icar.1993.1010

Katsova, M. M., & Livshits, M. A. 2011, Astronomy Reports, 55, 1123, doi: 10.1134/S1063772911120055

Kawashima, Y., Hu, R., & Ikoma, M. 2019, ApJL, 876, L5, doi: 10.3847/2041-8213/ab16f6

Kawashima, Y., & Ikoma, M. 2018, ApJ, 853, 7, doi: 10.3847/1538-4357/aaa0c5

Kiang, N. Y., Segura, A., Tinetti, G., et al. 2007, Astrobiology, 7, 252, doi: 10.1089/ast.2006.0108

King, G. W., Wheatley, P. J., Salz, M., et al. 2018, MNRAS, 478, 1193, doi: 10.1093/mnras/sty1110

Knutson, H. A., Howard, A. W., & Isaacson, H. 2010, ApJ, 720, 1569, doi: 10.1088/0004-637X/720/2/1569

Kopparapu, R. K. 2013, ApJL, 767, L8, doi: 10.1088/2041-8205/767/1/L8

Koskinen, T. T., Harris, M. J., Yelle, R. V., & Lavvas, P. 2013, Icarus, 226, 1678, doi: 10.1016/j.icarus.2012.09.027

Kostov, V. B., Schlieder, J. E., Barclay, T., et al. 2019a, AJ, 158, 32, doi: 10.3847/1538-3881/ab2459

—. 2019b, AJ, 158, 32, doi: 10.3847/1538-3881/ab2459

Kowalski, A. F., Hawley, S. L., Holtzman, J. A., Wisniewski, J. P., & Hilton, E. J. 2010, ApJL, 714, L98, doi: 10.1088/2041-8205/714/1/L98

Kreidberg, L., Bean, J. L., Désert, J.-M., et al. 2014, Nature, 505, 69, doi: 10.1038/nature12888

Kunimoto, M., & Bryson, S. 2020, Research Notes of the American Astronomical Society, 4, 83, doi: 10.3847/2515-5172/ab9a3c

Lam, K. W. F., Faedi, F., Brown, D. J. A., et al. 2017, A&A, 599, A3, doi: 10.1051/0004-6361/201629403

Lammer, H., Lichtenegger, H., Kulikov, Y., et al. 2007, AsBio, 7, 185, doi: 10.1089/ast.2006.0128

Line, M. R., Liang, M. C., & Yung, Y. L. 2010, ApJ, 717, 496, doi: 10.1088/0004-637X/717/1/496

Linsky, J. 2019, Host Stars and their Effects on Exoplanet Atmospheres, Vol. 955, doi: 10.1007/978-3-030-11452-7

Linsky, J. L., Yang, H., France, K., et al. 2010, ApJ, 717, 1291, doi: 10.1088/0004-637X/717/2/1291

Linsky, J. L., Wood, B. E., Youngblood, A., et al. 2020, ApJ, 902, 3, doi: 10.3847/1538-4357/abb36f

Lora, J. M., Kataria, T., & Gao, P. 2018, ApJ, 853, 58, doi: 10.3847/1538-4357/aaa132

Lothringer, J. D., & Barman, T. 2019, ApJ, 876, 69, doi: 10.3847/1538-4357/ab1485

Loyd, R. O. P., France, K., Youngblood, A., et al. 2016, ApJ, 824, 102, doi: 10.3847/0004-637X/824/2/102

—. 2018, ApJ, 867, 71, doi: 10.3847/1538-4357/aae2bd

Luque, R., Pallé, E., Kossakowski, D., et al. 2019, A&A, 628, A39, doi: 10.1051/0004-6361/201935801

Madhusudhan, N., Agúndez, M., Moses, J. I., & Hu, Y. 2016, SSRv, 205, 285, doi: 10.1007/s11214-016-0254-3

Maxted, P. F. L., Anderson, D. R., Collier Cameron, A., et al. 2013, PASP, 125, 48, doi: 10.1086/669231

Mazeh, T., Holczer, T., & Faigler, S. 2016, A&A, 589, A75, doi: 10.1051/0004-6361/201528065

Miguel, Y., & Kaltenegger, L. 2014, ApJ, 780, 166, doi: 10.1088/0004-637X/780/2/166

Miguel, Y., Kaltenegger, L., Linsky, J. L., & Rugheimer, S. 2015, MNRAS, 446, 345, doi: 10.1093/mnras/stu2107

Miller-Ricci Kempton, E., Zahnle, K., & Fortney, J. J. 2012, ApJ, 745, 3, doi: 10.1088/0004-637X/745/1/3

Modirrousta-Galian, D., Stelzer, B., Magaudda, E., et al. 2020, A&A, 641, A113, doi: 10.1051/0004-6361/202038280

Moses, J. I., Visscher, C., Fortney, J. J., et al. 2011, ApJ, 737, 15, doi: 10.1088/0004-637X/737/1/15

Murray-Clay, R. A., Chiang, E. I., & Murray, N. 2009, ApJ, 693, 23, doi: 10.1088/0004-637X/693/1/23

Narain, U., & Ulmschneider, P. 1996, SSRv, 75, 453, doi: 10.1007/BF00833341

Neupert, W. M. 1968, ApJL, 153, L59, doi: 10.1086/180220

Owen, J. E., & Jackson, A. P. 2012, MNRAS, 425, 2931, doi: 10.1111/j.1365-2966.2012.21481.x

Owen, J. E., & Lai, D. 2018, MNRAS, 479, 5012, doi: 10.1093/mnras/sty1760

Owen, J. E., & Wu, Y. 2016, ApJ, 817, 107, doi: 10.3847/0004-637X/817/2/107

Palle, E., Chen, G., Prieto-Arranz, J., et al. 2017, A&A, 602, L15, doi: 10.1051/0004-6361/201731018

Peacock, S., Barman, T. S., Schneider, A. C., et al. 2022, ApJ, 933, 235, doi: 10.3847/1538-4357/ac77f2

Pevtsov, A. A., Fisher, G. H., Acton, L. W., et al. 2003, ApJ, 598, 1387, doi: 10.1086/378944

Pidhorodetska, D., Moran, S. E., Schwieterman, E. W., et al. 2021a, AJ, 162, 169, doi: 10.3847/1538-3881/ac1171

—. 2021b, AJ, 162, 169, doi: 10.3847/1538-3881/ac1171

Pont, F. 2009, MNRAS, 396, 1789, doi: 10.1111/j.1365-2966.2009.14868.x

Poppenhaeger, K., & Wolk, S. J. 2014, A&A, 565, L1, doi: 10.1051/0004-6361/201423454

Richey-Yowell, T., Shkolnik, E. L., Schneider, A. C., et al. 2019, ApJ, 872, 17, doi: 10.3847/1538-4357/aafa74

Rugheimer, S., Kaltenegger, L., Segura, A., Linsky, J., & Mohanty, S. 2015, ApJ, 809, 57, doi: 10.1088/0004-637X/809/1/57

Salz, M., Schneider, P. C., Czesla, S., & Schmitt, J. H. M. M. 2015, A&A, 576, A42, doi: 10.1051/0004-6361/201425243

Sanz-Forcada, J., Micela, G., Ribas, I., et al. 2011, A&A, 532, A6, doi: 10.1051/0004-6361/201116594

Sato, B., Fischer, D. A., Henry, G. W., et al. 2005, ApJ, 633, 465, doi: 10.1086/449306

Schmitt, J. H. M. M., Haisch, B., & Barwig, H. 1993, ApJL, 419, L81, doi: 10.1086/187142

Schneider, A. C., & Shkolnik, E. L. 2018, AJ, 155, 122, doi: 10.3847/1538-3881/aaaa24

Schweitzer, A., Passegger, V. M., Cifuentes, C., et al. 2019, A&A, 625, A68, doi: 10.1051/0004-6361/201834965

Schwieterman, E. W., Kiang, N. Y., Parenteau, M. N., et al. 2018, AsBio, 18, 663, doi: 10.1089/ast.2017.1729

Segura, A., Kasting, J. F., Meadows, V., et al. 2005, AsBio, 5, 706, doi: 10.1089/ast.2005.5.706

Segura, A., Walkowicz, L. M., Meadows, V., Kasting, J., & Hawley, S. 2010, AsBio, 10, 751, doi: 10.1089/ast.2009.0376

Skaf, N., Bieger, M. F., Edwards, B., et al. 2020, AJ, 160, 109, doi: 10.3847/1538-3881/ab94a3

Smithsonian Astrophysical Observatory. 2000, SAOImage DS9: A utility for displaying astronomical images in the X11 window environment, Astrophysics Source Code Library, record ascl:0003.002. http://ascl.net/0003.002

Sohn, S. T., Bostroem, K. A., Proffitt, C., et al. 2019, STIS Data Handbook, Tech. Rep. 7, Space Telescope Science Institute

Spake, J. J., Sing, D. K., Wakeford, H. R., et al. 2021, MNRAS, 500, 4042, doi: 10.1093/mnras/staa3116

Stepien, K., & Ulmschneider, P. 1989, A&A, 216, 139

Szabó, G. M., & Kiss, L. L. 2011, ApJL, 727, L44, doi: 10.1088/2041-8205/727/2/L44

Teal, D. J., Kempton, E. M. R., Bastelberger, S., Youngblood, A., & Arney, G. 2022, ApJ, 927, 90, doi: 10.3847/1538-4357/ac4d99

Tian, F., France, K., Linsky, J. L., Mauas, P. J. D., & Vieytes, M. C. 2014, Earth and Planetary Science Letters, 385, 22, doi: 10.1016/j.epsl.2013.10.024

Tilley, M. A., Segura, A., Meadows, V., Hawley, S., & Davenport, J. 2019, Astrobiology, 19, 64, doi: 10.1089/ast.2017.1794

Traub, W. A. 2012, ApJ, 745, 20, doi: 10.1088/0004-637X/745/1/20

Venot, O., Fray, N., Bénilan, Y., et al. 2013, A&A, 551, A131, doi: 10.1051/0004-6361/201220945

Vidal-Madjar, A., Désert, J. M., Lecavelier des Etangs, A., et al. 2004, ApJL, 604, L69, doi: 10.1086/383347

Virtanen, P., Gommers, R., Oliphant, T. E., et al. 2020, Nature Methods, 17, 261, doi: 10.1038/s41592-019-0686-2

Wall, J., & Jenkins, C. 2003, Practical Statistics for Astronomers (Cambridge University Press), doi: https://doi.org/10.1017/CBO9780511536618

Wilson, D. J., Froning, C. S., Duvvuri, G. M., et al. 2021, ApJ, 911, 18, doi: 10.3847/1538-4357/abe771

Wood, B. E., Redfield, S., Linsky, J. L., Müller, H.-R., & Zank, G. P. 2005, ApJS, 159, 118, doi: 10.1086/430523

Woods, T. N., Chamberlin, P. C., Harder, J. W., et al. 2009, Geophys. Res. Lett., 36, L01101, doi: 10.1029/2008GL036373

Woods, T. N., Eparvier, F. G., Hock, R., et al. 2012, SoPh, 275, 115, doi: 10.1007/s11207-009-9487-6

Wright, N. J., Drake, J. J., Mamajek, E. E., & Henry, G. W. 2011, ApJ, 743, 48, doi: 10.1088/0004-637X/743/1/48

Wright, N. J., Newton, E. R., Williams, P. K. G., Drake, J. J., & Yadav, R. K. 2018, MNRAS, 479, 2351, doi: 10.1093/mnras/sty1670

Yelle, R., Lammer, H., & Ip, W.-H. 2008, SSRv, 139, 437, doi: 10.1007/s11214-008-9420-6

Youngblood, A., Pineda, J. S., Ayres, T., et al. 2022, ApJ, 926, 129, doi: 10.3847/1538-4357/ac4711

Youngblood, A., France, K., Loyd, R. O. P., et al. 2016, ApJ, 824, 101, doi: 10.3847/0004-637X/824/2/101

Zahnle, K., Marley, M. S., Freedman, R. S., Lodders, K., & Fortney, J. J. 2009, ApJL, 701, L20, doi: 10.1088/0004-637X/701/1/L20